ERRATA

ASHRAE Transactions, Vol. 105, Part 1

Several papers in the Transactions of the Chicago 1999 Winter Meeting were printed with incorrect figures. Following are corrected pages with the right figures in place.

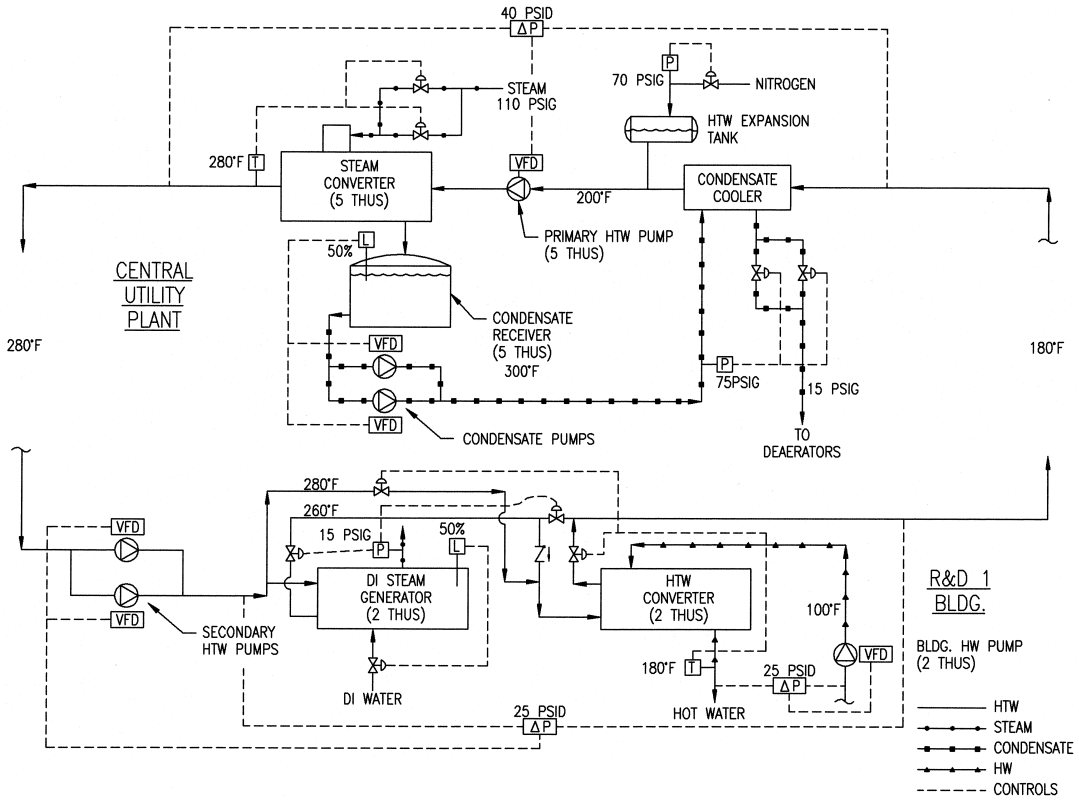

Figure 3 *High temperature water schematic.*

piping on elevated pipe support structures in order to avoid the potential corrosion and leakage issues associated with underground heating water distribution.

Also, 15.5% of the steam produced at peak wintertime operating conditions is distributed directly to the DMOS5-Phase II building adjacent to the central utility plant, and the remaining 4.5% is used by the deaerating feedwater heaters inside the central utility plant. (Although 280°F [132°C] high-temperature water distribution at a differential of 100 Btu/lb (233 kJ/kg) was the basis of the existing campus infrastructure, lower initial and operating costs were realized at the DMOS5-Phase II building by distributing 210 psi [1,448 kPa] [gauge] saturated steam at a differential of 1,000 Btu/lb [2,326 kJ/kg]). Condensate return from terminal devices is 100%, and the combined condensate stream entering the deaerating feedwater heaters averages 200°F (93°C) year-round. All pipeline condensate is "flashed" into lower pressure steam (Figure 2). In order to minimize steam distribution thermal losses, 210 psi (1,448 kPa) (gauge) saturated steam and 12 psi (83 kPa) (gauge) deionized steam pressures are reduced by as much as 10 psi (69 kPa) (gauge) and 4 psi (28 kPa) (gauge), respectively, during non-peak-heating conditions. Steam distribution leakage is controlled by daily monitoring of makeup water volume. All steam distribution utilizes above-ground, fiberglass-insulated piping on elevated pipe support structures in order to avoid the potential corrosion and leakage issues associated with underground steam distribution.

STEAM COST

Remaining challenges were to procure lower-priced fuel and power, plus apply cost-effective steam conservation and boiler plant efficiency measures, in order to minimize annual fuel and power costs. The latter challenge required evaluating the entire steam system (Figure 4) and targeting steam cost as the system's performance parameter:

$$C_{STM} = C_{BLR} + C_{FAN} + C_{PMP} \quad (1)$$

where C_{STM} is steam cost in \$/h, C_{BLR} is boiler fuel cost in \$/h, C_{FAN} is fan power cost in \$/h, and C_{PMP} is pump power cost in \$/h.

Respectively, the three steam cost constituents are given by

$$C_{BLR} = W_{STM} \times (H_{STM} - H_{FW}) \times C_{NG} / 1{,}020{,}000\ (37{,}998{,}000) \times e_{BLR} \quad (2)$$

where W_{STM} is the steam flow rate in lb/h (kg/h), H_{STM} is the steam enthalpy in Btu/lb (kJ/kg), H_{FW} is the feedwater enthalpy in Btu/lb (kJ/kg), C_{NG} is natural gas cost in \$/1,000 ft^3 (\$/1,000 m^3), and e_{BLR} is boiler efficiency.

Architecture for Intelligent Thermostats That Learn from Occupants' Behavior

Alex Boisvert **Ruben Gonzalez Rubio, Ph.D.**

ABSTRACT

This paper proposes a new approach to thermostat design. For many years, thermostats have been "dumb" devices, meaning that they react to their environment either by direct user control or by previous user programming. This new approach details an intelligent thermostat that learns about the behavior of the occupants and their environment and controls ambient temperature to maintain comfort according to human specifications. In that way, the thermostat reduces the number of interactions with the user and eliminates the need for them to learn how to program the device. Additionally, the thermostat reduces energy consumption by setback when occupants are absent. While the proposed architecture fundamentally changes the functionality of today's conventional thermostats, it retains their simple user interface.

This article presents the modular software architecture of this new intelligent thermostat design. The functionality of the thermostat in different states is described and how each module specializes in learning a certain pattern is explained. At the end, the results obtained using neural networks as a technique for learning are presented.

INTRODUCTION

Today, a growing number of economic and environmental considerations are leading us to look at new ways to reduce energy consumption. In northern regions, the activity that uses the most energy is the heating of buildings. To some extent, the same logic applies to regions where air conditioning is widely used. In this context, it is important to consider what determines the quantity of energy spent.

Figure 1 illustrates the thermal system under consideration. First, the external environment is uncontrollable and is

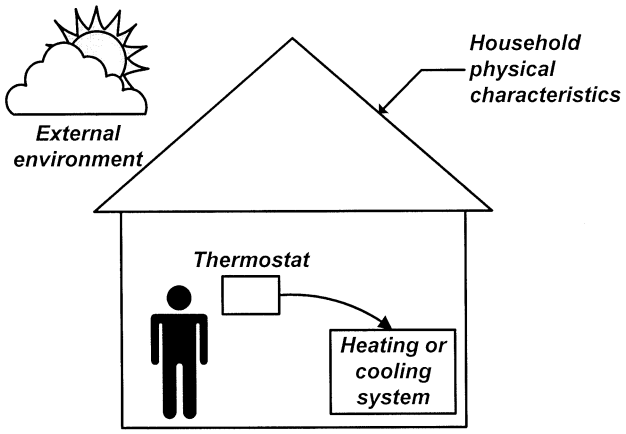

Figure 1 *Thermal environment.*

the most important factor that influences energy consumption. Second, the physical building characteristics are important, but in most cases they are adequate and fixed. Third, a thermostat is used to monitor ambient temperature and control a heating or cooling system. Finally, one or more occupants operate the thermostat to obtain a given ambient temperature that reflects their thermal comfort.

In this view, a person interacts with a thermostat, which, in turn, interacts with a heating/cooling system. In our mind, it is this interaction that mostly influences energy consumption. Occupants are often lazy about frequently adjusting their thermostats. Also, Harmon (1981) argues that "many people do not fully understand the proper operation of the most common residential thermostat." For these reasons, the authors designed an intelligent thermostat that automates comfort control and energy conservation.

Alex Boisvert is a graduate student and **Ruben Gonzalez Rubio** is a professor in the département de génie électrique et de génie informatique, Université de Sherbrooke, Québec, Canada.

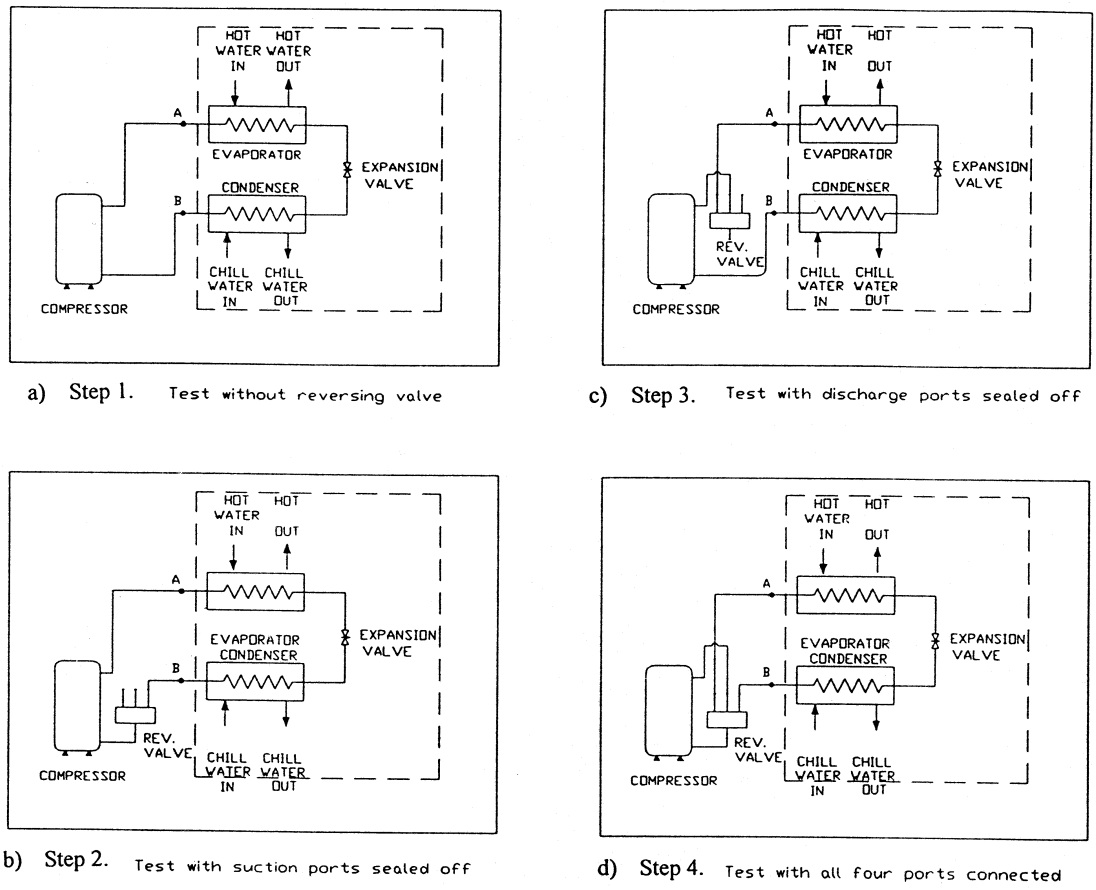

Figure 4 *Schematic of experimental procedure, steps 1 through 4 (Krishnan 1986).*

TABLE 2
Points A and B Conditions for Both R-410a and R-22 Tests

Point Condition	Pressure kPa (std. deviation)	Temperature °C (std. deviation)	Pressure psia (std. deviation)	Temperature °F (std. deviation)
Point A (R-410a) Exiting Evaporator	900.7 (4.1)	10.1 (0.5)	130.6 (0.60)	50.2 (0.48)
Point B (R-410a) Entering Condenser	2420.7 (1.2)	73.2 (0.80)	351.0 (0.17)	163.8 (1.4)
Point A (R-22) Exiting Evaporator	650.5 (3.1)	11.7 (0.14)	94.3 (0.45)	53.0 (0.25)
Point B (R-22) Entering Condenser	1741.4 (3.0)	82.6 (1.1)	252.5 (0.43)	180.7 (2.0)

Discharge pressure drops were found to be between 8.3 kPa and 12.3 kPa (1.2 psi and 2.0 psi) for the R-410a tests and between 11.8 kPa and 20.7 kPa (1.7 psi and 3.0 psi) for R-22. Higher pressure drops were associated with smaller valves. Similarly, suction-side pressure drops were 3.3 kPa to 4.3 kPa (0.5 psi to 0.6 psi) and 4.7 kPa to 7.8 kPa (0.7 psi to 1.1 psi) for the R-410a and R-22 tests, respectively. The lower pressure drop in R-410a tests was attributed primarily to the reduction in refrigerant mass flow rate and lower vapor velocities. Measurements showed that the mass flow rate was reduced from 49.7 g/s (394.4 lbm/h) without a reversing valve installed to an average of 46.3 g/s (367.5 lbm/h), or a 6.8% reduction, with a reversing valve. Since the change in enthalpy across the evaporator did not change significantly

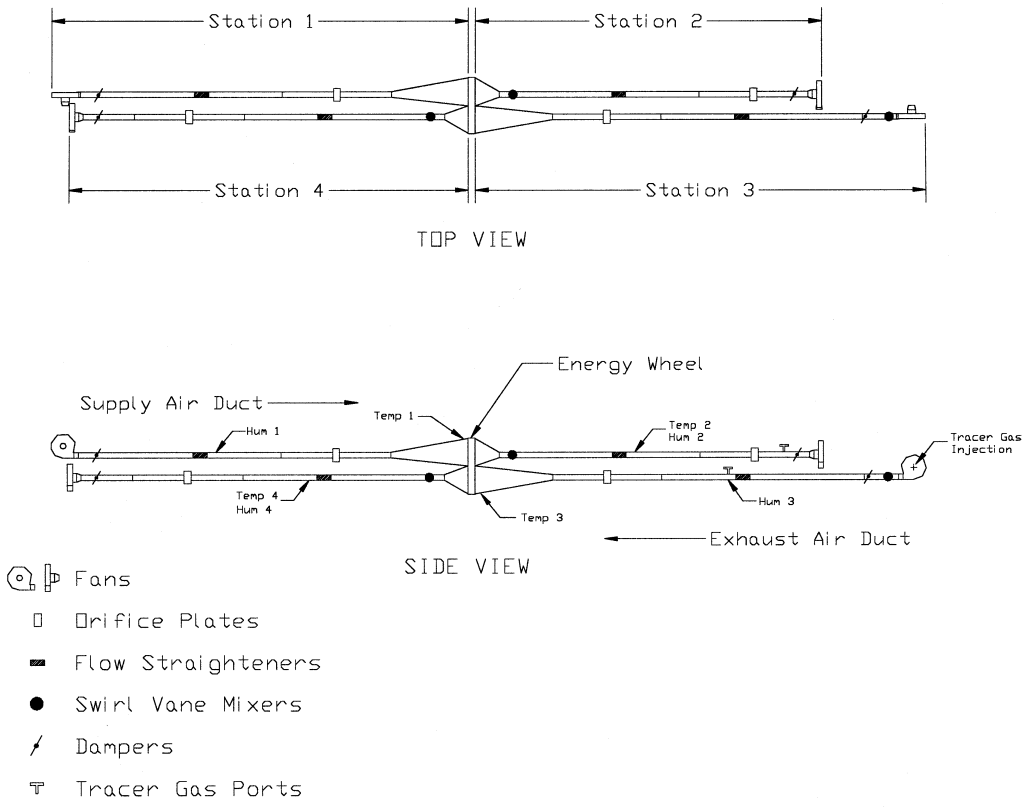

Figure 2 *The laboratory-test facility used in this analysis.*

TABLE 2
Properties of the Energy Wheel Used in the Tests

WHEEL	M = 13.5 kg	L = 0.102 m	diameter = 0.92 m
Speed = 20 rpm	D_h = 1.20 mm	porosity = 82%	Nu = 2.39 (fully developed)
DESICCANT	ρ = 350 kg/m^3	Cp= 615 J/(kg·K)	mass fraction = 22%
σ_d = 0.69	Wm = 0.13	C = 40	η = 0.05

sensible and latent effectivenesses. The prime cause of these uncertainties is the uncertainty of the input data used for the wheel that was tested because the numerical variations due to the numerical algorithm were less than ±0.5% (Simonson and Besant 1997b).

LABORATORY EXPERIMENTS

The laboratory-experimental test facility (Figure 2) was designed in accordance with ASHRAE Standard 84-1991, which details the equipment and analysis necessary to achieve standardized results for air-to-air energy recovery devices. This facility differs slightly from the standard in the measurement of airflow rates and relative humidities as well as the method of providing for fan-driven airflows. The energy wheel used in the experiments is a commercial wheel with a design mass flow rate of air of 0.5 kg/s (1.5 kg/[s·m^2]) and an expected pressure drop across the wheel of 50 Pa (Johnson et al. 1998). The properties of the molecular sieve coated energy wheel are given in Table 2. The energy wheel is constructed of 0.042 mm thick aluminum that is coated on both sides with 0.046 mm of molecular sieve desiccant. the sine wave pores in the matrix (Figure 1b) have a height of 4.75 mm and a wave length of 1.65 mm.

In the laboratory experiments, the wheel was divided into quadrants and the air flowed through opposing quadrants, as shown in Figure 3. This configuration retains similar face velocities as the original design operating conditions while reducing the crossover leakage between the two airstreams and the required airflow rate. Consequently, the capacity required for the heating and cooling equipment and fans was reduced. A unique feature of the test facility to reduce contamination, which is not a part of ASHRAE Standard 84-1991, is the use of four fans instead of two (Figure 2). Four fans were used in the tests to keep the pressure at the wheel near atmospheric pressure and to provide independent control over the

initial rule set is set up for a controlled plant with assumed properties (quick response or slow response). Then the STFLC will improve itself to obtain optimal behavior. A dashed curve AB in Figure 2a indicates a performance trajectory deviating a little bit from the desired path such that it will enter into the left-half part of the linguistic plane, resulting in oscillation and overshoot. The dashed curve AC indicates a performance trajectory deviating to the other side of the desired path. The key objectives of the self-tuning strategy proposed in this study are to measure the deviation of the performance trajectory from the desired one and to improve the relevant rules or scale factors to eliminate the deviation.

In real applications, the desired performance trajectory is established based on operating experience and knowledge about fuzzy logic systems. In this work, the desired trajectory for the heating mode, shown in Figure 2a with AO, goes from point A to point D where the derivative error (d) has a large value that results in the controlled parameter (T) responding quickly. Then the system approaches the stable point O along a smooth path.

The whole performance trajectory can be divided into four stages located in four areas marked 1, 2, 3, and 4 in Figure 2a. In area 1, point E is chosen as a reference point and the performance is then measured by the distance d_e, which is defined as the shortest distance from point E to the smoothed trajectory. A smaller d_e results in a slower dynamic response, while a larger d_e results in a faster response in the first stage. In area 2, point F is chosen as a reference point and the performance in the second stage then can be measured by the distance d_f between point F and the trajectory. In this area, a smaller d_f results in a faster dynamic response, while a larger d_f results in a slower response. A very small d_f may result in overshoot in the dynamic process. Using the same analysis, points G and H are chosen as the reference points for areas 3 and 4, respectively, and d_g and d_h are used as the criterion to measure the performances of the STFLC in the third and fourth stages. Larger d_g and smaller d_h can lead to static error where the derivative of the error goes to zero before the error does. The performance measurement strategies are summarized in Table 1.

MODIFICATION PROCEDURE

There are two types of modification strategies: modifying the fuzzy subsets of the control rules or modifying the elements of the look-up table.

TABLE 1
The Performance Measurement Strategies for the Proposed STFLC

Stage	Reference	Criterion	Smaller Value	Larger Value
1	E	d_e	Slow response	Possible overshoot
2	F	d_f	Possible overshoot	Slow response
3	G	d_g	Overshoot	Static error
4	H	d_h	Static error	Overshoot

Replacing an old fuzzy control rule with a new one results in revising the fuzzy relation matrix. This involves detailed fuzzy mathematical calculations. If an old control rule expressed as a fuzzy matrix $R_{k,old}$ (Huang and Nelson 1994a, 1994b) is replaced by a new rule expressed as a fuzzy matrix $R_{k,new}$, the general relation matrix R_g can be revised as

$$R_{g,\,new} = [R_{g,\,old} \cap \underline{R}_{k,\,old}] \cup R_{k,\,new} \quad (1)$$

where $\underline{R}_{k,old}$ is the fuzzy complementary matrix of $R_{k,old}$. The complementary operation on $R_{k,old}$ and the intersection operation with $R_{g,old}$ signify "elimination" of the obsolete rule from the general relation matrix. The union operation with $R_{k,new}$ signifies "appending" the new rule to the general relation matrix. Modifying fuzzy control rules is time-consuming and demands substantial computer storage.

For a given set of control rules, the control policy is usually expressed by a control surface (Huang and Nelson 1994a, 1994b), which is expressed in terms of fuzzy subsets. Each cell in the control surface indicates the fuzzy value of the control action. Figure 3a presents the control surface for a control rule set in terms of fuzzy subsets. A control surface can also be expressed in terms of the elements of a look-up table.

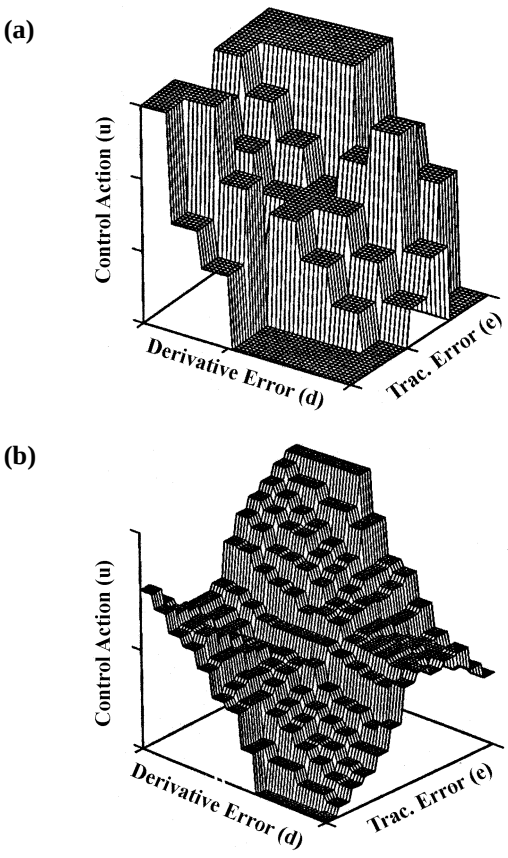

Figure 3 *Two types of control surfaces for a fuzzy control rule set: (a) control surface in terms of fuzzy subsets; (b) control surface in terms of elements.*

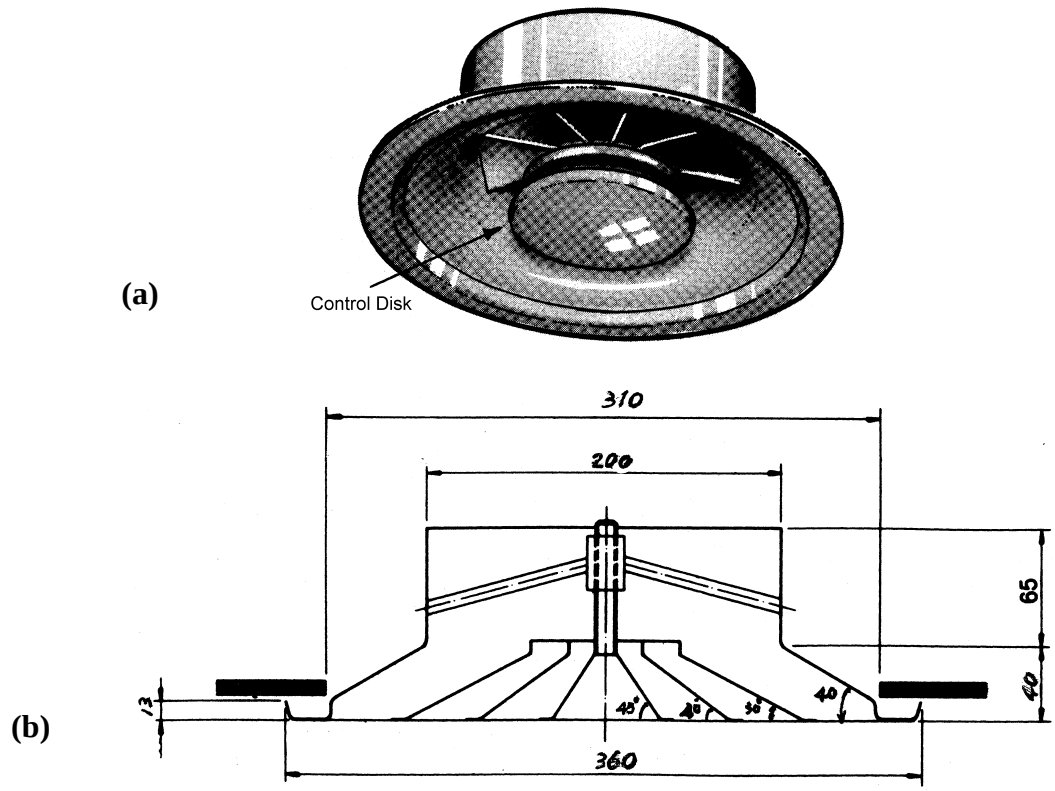

Figure 2 *(a) Vortex diffuser, (b) multi-cone circular diffuser.*

airflow pattern and air turbulence in rooms. The flow patterns and air turbulence are generated primarily by air jets and secondarily by internal heat loads. These effects are dependent on the temperature of the supply air. There is an extensive body of literature concerning chilled air distribution, but there is very limited information available on indoor airflow and temperature measurements for cold air distribution systems.

Knebel and John (1993) conducted several field tests and showed that cold air can be successfully supplied to a room to produce a comfortable indoor environment under most operating conditions by using the nozzle-type diffusers. However, the performance of the associated jet and the resulting field velocities and temperatures are not given. Kondo et al. (1995) performed a laboratory study for cold air distribution systems with a multi-cone circular diffuser. They concluded that there are only minor differences in velocity and temperature distributions between an 8°C (46°F) cold air system and a 13°C (55°F) conventional system with the same room temperature. However, substantial condensation and dumping were observed for the 8°C (46°F) cases. Shioya et al. (1995) studied the thermal comfort aspect of a cold air distribution system using a thermal mannequin. Their work indicates that circular ceiling diffusers gave a higher degree of comfort than linear slot diffusers in a similar situation. However, selection and positioning of the diffusers was critical to ensure that the diffused air velocity remained satisfactory. Hassani and Stetz (1994) investigated the effect of local loads on the behavior of cold air jets with early separation using an infrared visualization technique to record the temperature distribution. Knappmiller and Kirkpatrick (1994) and Kirkpatrick and Knappmiller (1996) have used the computational fluid dynamics (CFD) technique to study cold air jet behavior and the associated indoor thermal comfort index. Rose and Seymour (1993) have provided some guidance as to the best implementation of cold air distribution with slot-type diffusers using CFD analysis. Shakerin and Miller (1995) tested two types of vortex diffusers under isothermal conditions. Somewhat more induction was observed compared with that of a multi-cone circular diffuser in their study.The authors are unaware of any other work on the subject of high-induction cold air jets and their associated room air distribution pattern.

The objectives of the study described here were, therefore, (1) to study the flow pattern and temperature distribution of nonisothermal jets issuing from a multi-cone circular ceiling diffuser, a nozzle-type diffuser, and a vortex diffuser, (2) to compare the performances of these diffusers and the associated room thermal comfort index under the condition of supplying cold air, and (3) to provide some useful suggestions for modifying the currently available multi-cone circular ceiling diffuser to fit the performance requirements of cold air distribution.

EXPERIMENTAL SETUP

A full-scale environmental chamber 7.2 m (length) × 4.2 m (width) × 2.8 m (height) was constructed following ISO Standard 5219 (ISO 1984) and ASHRAE Standard 113

assumed for the theoretical calculation of the COP of absorption heat transformers. The effectiveness of the intermediate heat exchanger was assumed to be 1.0. The work required to pump the strong solution and liquid working medium to the high-pressure side of the cycle is negligible. Heat losses to the surroundings, as well as pressure drops due to friction, etc., were assumed to be negligible.

In general, an absorption heat transformer is designed to feed a large amount of exhaust heat at an intermediate temperature level to the generator and evaporator as the driving heat source and, at the same time, supply cooling water to the condenser. It thus takes heat of higher temperature out of the absorber by making use of the temperature difference between the exhaust heat and the cooling water as the driving force. Figure 1 shows a schematic diagram of a single-stage absorption heat transformer. Its coefficient of performance is expressed by the following equation:

$$COP = Q_A/(Q_G+Q_E) = Q_A/(Q_A+Q_C) = 1/(1+Q_C/Q_A)$$

Operating Range

Figure 2 shows operating ranges for the various working medium+absorbent systems used. In comparison with the H_2O+LiBr system, the H_2O+LiBr+$LiNO_3$ system showed a wide operating range in the higher temperature range of the generator, which is concluded to have occurred because the solubility is larger for the latter system than for the former system in the higher temperature range. The H_2O+LiCl+$LiNO_3$ system showed a narrow operating range in the lower temperature range of the generator due to the low solubility of this system. The operating range shown by the H_2O+LiI+$LiNO_3$ system was somewhat wide, even in the lower temperature range of the generator, and increased considerably with an increase in the temperature of the generator. This is concluded to have occurred because the solubility of this system is high even in the lower temperature range and is still higher in the higher temperature range. The systems H_2O+$Ca(NO_3)_2$+$LiNO_3$, H_2O+$Ca(NO_3)_2$+$LiNO_3$+KNO_3, and H_2O+$LiNO_3$+$NaNO_3$+ KNO_3 were found to have a narrow operating range within the entire temperature range of the generator, compared with the H_2O+LiBr system.

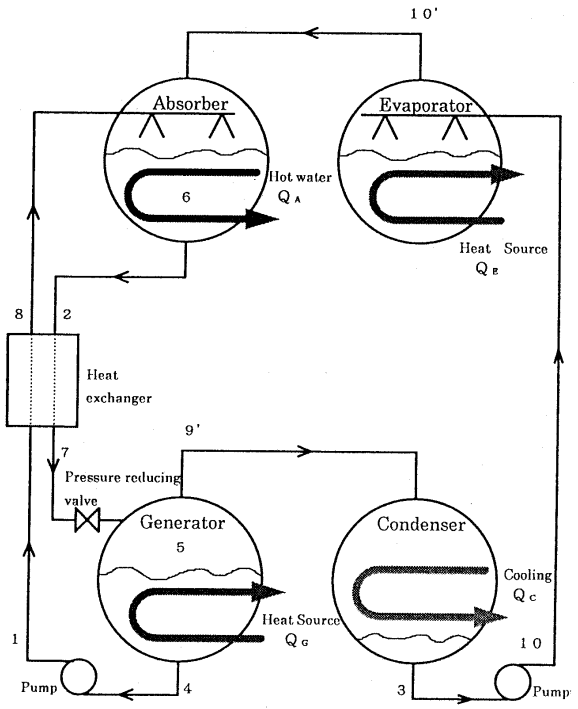

Figure 1 *Schematic diagram of single-stage absorption type.*

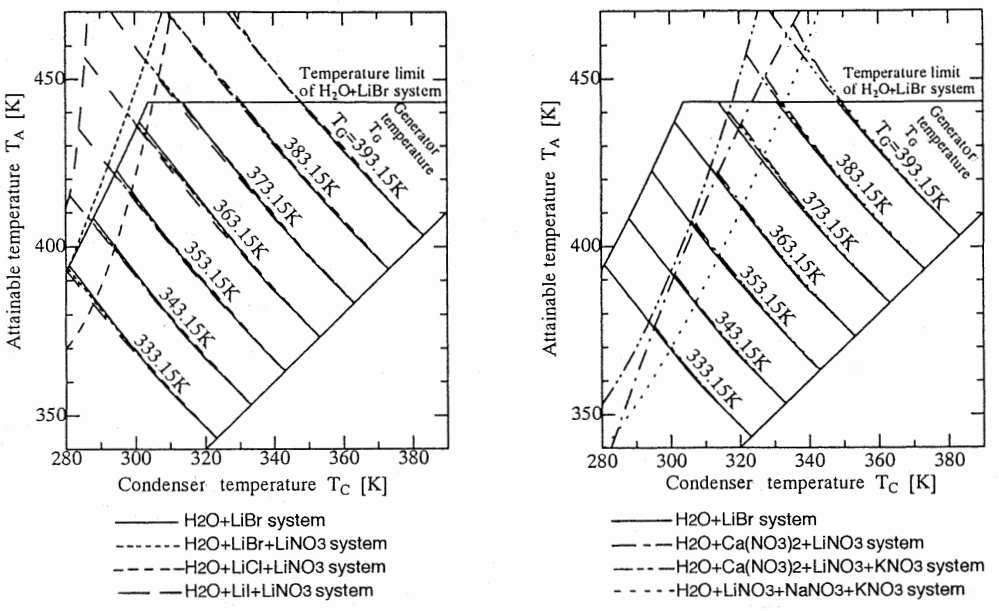

Figure 2 *Comparison of operating range of various systems for single-stage absorption type.*

TABLE 4
Fresh Food Cycle Optimization Data (TL2.5F Compressor)

Refrigerant	Refrigerant Charge (g)	Temperature (°C)*			Pressure (kPa)*		Energy kWhd	Run Time % On
		Tff-a	Tffe-i	Tffe-o	Pffcp-i	Pffcp-o		
R-134	111.60	7.67	0.41	7.45	248.15	732.35	0.76	5.18
	125.70	7.72	2.39	7.14	246.34	743.40	0.63	5.90
	145.60	7.87	3.70	5.62	233.44	750.41	0.60	12.39
	161.70	7.96	4.11	4.06	225.62	787.29	0.63	22.41
	179.30	7.93	4.30	3.65	225.90	783.19	0.62	23.18
	201.30	7.92	4.42	3.28	228.69	796.08	0.79	31.25
R-227ea	139.50	7.67	−0.48	7.54	223.45	617.07	0.80	3.47
	164.30	7.75	2.71	7.00	227.84	628.94	0.70	4.97
	182.70	7.86	4.22	4.95	227.51	647.91	0.66	6.58
	201.90	7.91	4.48	3.97	223.22	654.38	0.67	8.64
	228.10	7.87	4.89	3.38	218.04	664.26	0.68	12.03
R-134a	159.00	7.70	3.55	4.26	272.86	1005.37	0.58	20.49
	100.20	7.61	−1.96	7.69	219.88	945.78	0.84	14.36
	118.40	7.63	1.12	7.64	222.22	980.50	0.67	26.62
	140.40	7.63	2.95	5.55	254.99	994.00	0.60	21.95
	189.10	7.81	3.64	3.60	281.68	1014.85	0.64	22.28
	174.10	7.74	3.57	3.69	276.07	1014.85	0.61	21.23
	216.90	7.85	3.83	3.26	294.06	1043.76	1.01	33.70

* fz = freezer, ff = fresh food, a = average, i = in, o = out, e = evaporator, cp = compressor, kWhd = kWh/day.

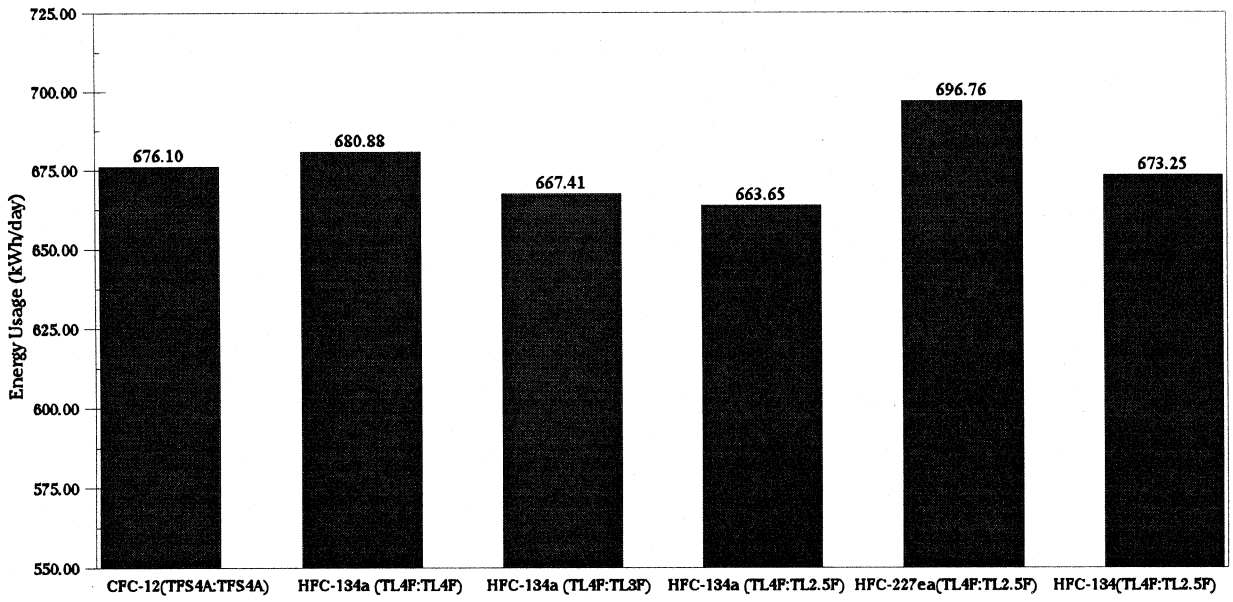

Figure 4 *Energy consumption using various compressors.*

level, $(K{\cdot}A)_{drop}$, is evaluated by assuming the Lewis equation as unity approximately (Bernier 1995) as follows:

$$(K \cdot A_i)_{\text{drop}} = \frac{0.5 \cdot m_{ev}}{0.001 \cdot C_{pm} \cdot (W_{i,av} - W_{av})} \tag{22}$$

where $W_{i,av}$ is the moisture content of the saturated air, which is evaluated at T_w. C_{pm} indicates the average specific heat of the moist air, in J/(kg_{da}·K), which can be determined as follows:

$$C_{pm} = C_{pa} + W_{av} \cdot C_{pv}. \tag{23}$$

Finally, the coefficient of performance of the countercurrent cooling towers (the available NTU) can be predicted by adding Equation 21 into Equation 22:

$$\text{NTU}_{av} = \frac{(K \cdot A_i)_{\text{total}}}{m_{w,1}} = \frac{(K \cdot A_i)_{\text{fill}} + (K \cdot A_i)_{\text{drop}}}{m_{w,1}}. \tag{24}$$

On the other hand, the thermal demand equation (Ünsal and Varol 1990) can be revised by considering the evaporation, and a simple prediction formula for the sizing of the countercurrent cooling tower can be written by considering the evaporation as follows:

$$\text{NTU}_{\text{req}} = \frac{M_2}{M_1} \cdot \frac{C_{pw}}{(n-1)} \cdot 1n\left\{1 + \frac{(i_2 - i_1) \cdot (n-1)}{i_{i,1} - i_1}\right\} \tag{25}$$

The required NTU calculated by this formula indicates a realistic thermal demand for a specific cooling duty.

EXPERIMENTAL SETUP

A bench-top laboratory cooling tower of the vertical type was used to conduct experiments for determination of the coefficient of performance of the countercurrent cooling tower shown in Figure 2. The cooling tower had fill characteristics, a, of 110 (m^2/m^3). The entering water mass flow rate range, $m_{w,1}$, was between 0 kg/s and 0.05 kg/s. The cooling load was generated by an electrical resistance heater selector of 0.5 kW, 1 kW, and 1.5 kW. Temperature was recorded by a 0.1°C sensitive digital thermometer. The airflow rate was controlled by an air damper and measured by a venturimeter. The maximum dry airflow rate was approximately 0.06 kg/s depending on the moisture content and specific volume of the moist air exiting the cooling tower. The water flow rate was controlled by a throttle valve and measured by an orificemeter with a sensitivity of 0.001 kg/s. Makeup water was supplied by a tank, and the water level in the cooling tower water circulation tank was kept constant to achieve steady state in the cooling circuit. The wet-bulb temperature of the air was kept constant during the experiments.

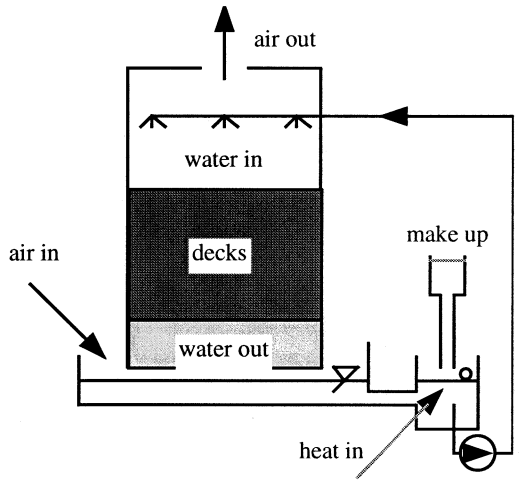

Figure 2 *Schematic representation of the cooling tower used in the experiment.*

The actual available NTU of the cooling tower was obtained by performing a series of experiments using the Carey-Williamson Method (Gurner and Cotter 1977) as

$$\text{NTU}_{av} = \frac{C_{pw} \cdot (T_{w,2} - T_{w,1})}{\Delta i_m}, \tag{26}$$

where the corrected enthalpy driving potential, Δi_m, is expressed as follows:

$$\Delta i_m = f \cdot \gamma_m \tag{27}$$

and

$$\gamma_m = i_{i,m} - i_m \tag{28}$$

where f is the correction factor of the arithmetic mean of the enthalpy driving potential, γ_m (see Figure 3).

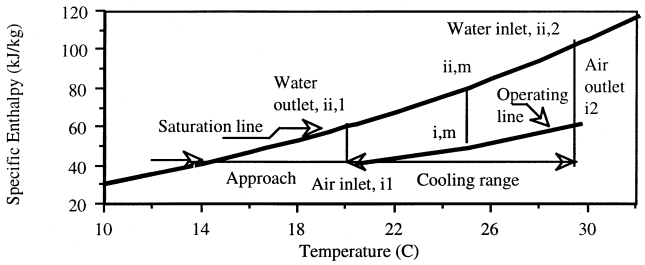

Figure 3 *Diagram of enthalpy driving potential.*

Mean value of the saturated air enthalpy is evaluated at the arithmetic mean of the inlet and exit water temperatures. Mean value of the air enthalpy is evaluated at the arithmetic mean of the tower inlet and the exit air wet-bulb temperatures. f can be evaluated from the Carey and Williamson chart (Gurner and Cotter 1977) as a function of the enthalpy driving potential at the inlet and the exit states of the cooling tower, which are

$$\gamma_1 = i_{i,2} - i_2 \tag{29}$$

$$\gamma_2 = i_{i,1} - i_1 \tag{30}$$

Q_l = heat generated by the overhead lighting,

Q_{ex} = heat from exterior walls and windows and the transmitted solar radiation.

Since there is a temperature stratification in a room with displacement ventilation, the ceiling and floor surface temperature are unknown. In this investigation, we use the two temperatures in the CFD program to calculate the air temperature and contaminant distributions. Following is a discussion of a procedure used to estimate the temperatures.

In a space with displacement ventilation as shown in Figure 6, the steady-state heat balance on the surfaces of the floor and the ceiling can be expressed as

$$Q_{af} = Q_{sf} + Q_{rf} + Q_{of}, \tag{6}$$

$$Q_{ac} = -Q_{sc} + Q_{rc} + Q_{oc}\,, \tag{7}$$

where

Q_{af} = convective heat transfer from the floor to the air,

Q_{sf} = radiative heat transfer from the heat sources to the floor,

Q_{rf} = radiative heat transfer from the ceiling and walls to the floor,

Q_{of} = heat transfer from the space under the floor to the floor surface,

Q_{ac} = convective heat transfer from the air to the ceiling,

Q_{sc} = radiative heat transfer from the heat sources to the ceiling,

Q_{rc} = radiative heat transfer from the ceiling to the walls and floor,

Q_{oc} = heat transfer from the ceiling surface to the space above the ceiling.

Further, Newton's law reads:

$$Q_{af} = \alpha_{cf}\,(T_{fs} - T_f)A, \tag{8}$$

$$Q_{ac} = \alpha_{cc}\,(T_c - T_{cs})A, \tag{9}$$

where

α_{cf} = convective heat transfer coefficient on the floor,

T_{fs} = floor surface temperature,

T_f = air temperature near the floor,

α_{cc} = convective heat transfer coefficient on the ceiling,

T_{cs} = ceiling surface temperature,

A = floor/ceiling area.

The convective heat transfer on the floor causes an air temperature increase from the supply temperature to the air temperature on the foot level. Therefore,

$$Q_{af} = \rho C_p\, V(T_f - T_s). \tag{10}$$

The radiative heat transfer from the heat sources to the floor and the ceiling, respectively, may be estimated by

$$Q_{sf} = \sum_j r_{fj} Q_j\,, \tag{11}$$

$$Q_{sc} = \sum_j r_{cj} Q_j\,, \tag{12}$$

where

Q_j = heat emitted by jth heat source, including transmitted solar radiation;

r_{fj} = fraction of radiative heat transfer from jth heat source to the floor;

r_{cj} = fraction of radiative heat transfer from jth heat source to the ceiling.

The r_{fj} and r_{cj} need to be estimated from the room geometry.

According to Mundt (1996), the radiative heat transfer from the ceiling and walls to the floor, Q_{rf}, and the radiative heat transfer from the ceiling to the floor and walls, Q_{rc}, can be estimated via

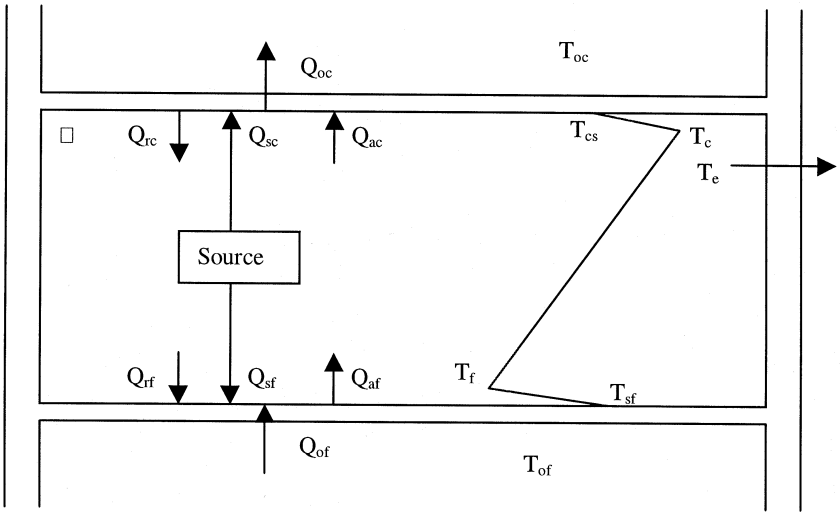

Figure 6 *Heat transfer in a space with the displacement ventilation.*

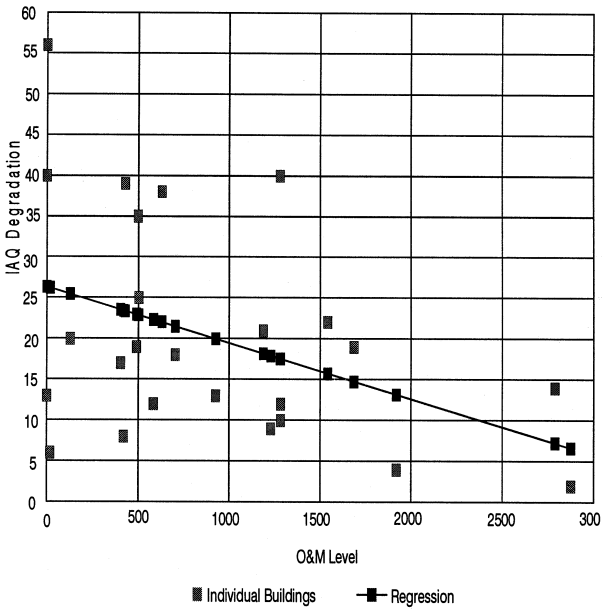

Figure 2 *IAQ/O&M trend.*

level and IAQ are statistically significant (p-values <0.05). These trends were obtained through analysis of a sample of office buildings in the Chicago metropolitan area. However, the trends indicate similarities throughout the United States and Canada. The statistical analysis also recognized the fact that larger buildings typically have more components and would have higher O&M levels. This was accomplished through a statistical comparison of IAQ information from small and large buildings, which was independent of size, outdoor ventilation rates, and space temperature.

STANDARD SOP STRUCTURE

A standard SOP structure was developed to ensure consistency. Three levels of SOPs were developed:

- Building
- System
- Component

The system level will generally be sufficient for most buildings; however, complex buildings may also require SOPs for components and the whole building. The SOP development strategy and structure developed in the guide (Dorgan et al. 1998b) concentrate on the system level; however, the strategy and structure apply to all three SOP levels.

Information from O&M personnel and *ASHRAE Guideline 4-1993* provided the basis for the SOP structure. The SOP documentation consists of seven sections. The first section includes basic information on the system, building, or component being addressed. The other sections provide information on how to evaluate and the correct action to take if required.

Section 1: General Information

This section provides a short description of the building, system, or component to be addressed in the SOP. Documenting the Design Intent provides an important resource for understanding system operation and limitations. System SOP information contained in this section includes:

- System type
- Area served
- Control description
- Associated systems or components

Section 2: Standards of Performance

The criteria used to evaluate the SOPs are developed in Section 2. The evaluation process meets the SOP requirement of ensuring that "a building, system, or component is operating properly —determined through a series of measurements." The criteria may be taken from existing standards (ASHRAE for example), local codes/guidelines, or manufacturer's information. The criteria may be measured or subjective. The criteria used for evaluation vary by season (summer/winter) or by occupancy mode (unoccupied/occupied). Examples of SOP criteria are:

- The energy efficiency for a chiller is less than 0.6 kW/ton (0.017 kW/kW_T) full load and 0.7 kW/ton (0.020 kW/kW_T) at 50% load.
- The IAQ in a conference room meets the requirements of *ANSI/ASHRAE Standard 62-1989* for CO_2 levels.

Section 3: Information to be Recorded

Measurements must be taken to determine if SOPs are met. The validity and usefulness of the measurements require that the frequency, accuracy, number, references, and other details be determined.

An example of the measurements required for the chiller EER SOP discussed in Section 3 are:

- Entering and leaving chilled-water temperatures
- Chilled-water flow rate
- Energy input

The same measurements can be used in more than one SOP, which allows for the actual list of required measurements to be reduced.

Section 4: Calculations

The measurements are used to ascertain that the SOPs are being met. This is accomplished through calculations involving the information recorded in Section 3. Calculations may be easily automated through computerized scheduling and tracking systems.

Equation 1 is an example of a calculation for determining the chiller EER.

TABLE 1
Room Dimensions in Meters (Feet) for CFD Simulations

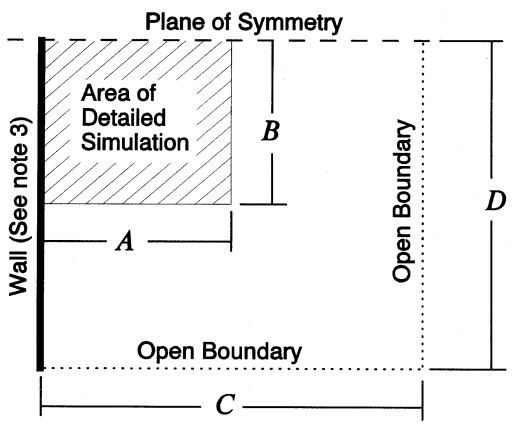

Open plan room (O)

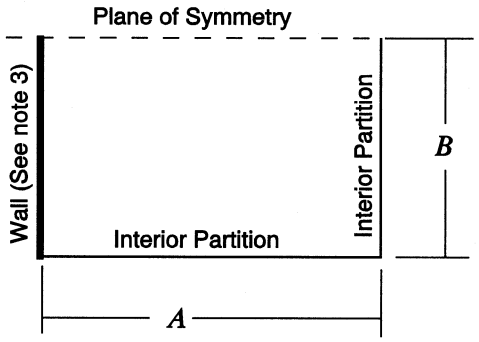

Enclosed room (E)

Notes:
1. *H* is floor to ceiling height.
2. NA is not applicable.
3. Wall is an exterior wall for rooms O2, E3, and E4; it is interior partition for rooms O1, E1, E2 and E5.

Room Type	A	B	C	D	H
O1	4.6 (15)	4.6 (15)	9.2 (30)	9.2 (30)	2.74 (9.0)
O2	5.5 (18)	3.91 (13)	10.5 (34)	9.09 (30)	2.74 (9.0)
E1	4.6 (15)	4.6 (15)	N/A	N/A	2.74 (9.0)
E2	4.6 (15)	3.0 (9.8)	N/A	N/A	2.74 (9.0)
E3	4.6 (15)	1.71 (5.6)	N/A	N/A	2.74 (9.0)
E4	4.6 (15)	2.56 (8.7)	N/A	N/A	2.44 (8.0)
E5	6.0 (20)	2.3 (7.5)	N/A	N/A	2.44 (8.0)

area is very large as is the case for open plan offices, and enclosed rooms are ones that are relatively small with walls like those of private offices. For these rooms, the fire locations and the arrangements of HVAC supplies and returns are shown in Figure 1.

MODELING APPROACH

A commercially available computational fluid dynamics (CFD) model was used to perform the numerical simulations. This model (CFC 1995) is an upgrade of the one used for simulations in the second year of this project, and the only upgraded features relevant to the simulations of this study consist of simplified data input.

A detailed description of CFD modeling is beyond the scope of this report. The nonmathematical descriptions in the following sections are intended to provide an explanation of the assumptions of the simulations of this paper and to provide insight for those not familiar with the field. The user's manual (CFD 1995) provides the exact equations and mathematical definitions that apply to these simulations. For more information about CFD modeling, readers are referred to Abbott and Basco (1989), Anderson et al. (1984), Hirsch (1990), Hoffmann (1989), and Kumar (1983). For general information about fluid dynamics, readers are referred to Schetz (1993), Schlichting (1960), Sherman (1990), White (1974), and Yuan (1967).

CFD Concept

The CFD modeling consists of dividing the flow field into a collection of small rectangular cells and determining the flow at each cell by numerically solving the governing conservation equations of fluid dynamics. Boundary conditions are prescribed for walls, floor, ceiling, HVAC supplies, HVAC returns, openings to the outside, and planes of symmetry. For this project, all the CFD simulations were unsteady, using the calculated properties from one time step to calculate those of the next time step. At the start of a simulation, each cell can be set to zero flow conditions or conditions read into the computer from a previous simulation. Zero flow conditions consist of zero velocity and ambient pressure and temperature. To generate fire-induced flows, heat is released in several control volumes over time.

The governing equations of fluid dynamics describe the motion of fluid throughout the flow field. These equations are

ments for fixed guideway transit systems. NFPA 130 requires emergency ventilation in stations and tunnels to protect the passengers and employees from a fire or smoke generation. The criteria specified in the standard are as follows:

- The emergency ventilation system shall produce airflow rates to provide a stream of noncontaminated air to passengers and employees in a path of egress away from a train fire and to prevent back-layering of smoke in a path of egress away from a train fire.
- The maximum temperature in the path of evacuation shall not exceed 60°C, ignoring radiant heating effects.
- The air velocity in the path of evacuation shall not exceed 11 m/s; air velocities above this level may cause difficulty in walking.

To preclude imposing requirements on older existing transit systems, which may be impractical and/or cost prohibitive, NFPA 130 does not mandate that existing systems comply with these ventilation requirements. Almost all of the Buenos Aires Metro was built long before NFPA 130 was issued. The system has for many decades provided safe and reliable service. Major fires that would require ventilation systems to assist passenger safety have been rare over the history of the transit system. However, Buenos Aires Metro plans to improve the subway ventilation based on NFPA 130 with priority given to meeting the requirements for low-intensity fires throughout the subway system. For new subway systems, recommendations are for the high-intensity fire of a train fully engulfed in fire.

Fire Heat Release Rate

The train fire heat release rate used for the analysis was a low-intensity fire of 1.8 MW (NYC 1994). This value corresponds to a train fire that involves only the undercar combustible contents.

VENTILATION ALTERNATIVES

The analysis of alternative ventilation strategies focused initially on identifying and evaluating the potential use of various strategies that have been used successfully in the industry. These strategies include (1) end-of-station fan plants, (2) mid-tunnel fan plants, (3) propeller fans, (4) jet fans, and (5) station mechanical ventilation. In evaluating these strategies, careful consideration was given to space constraints for locating equipment within and around the stations, cost-effectiveness, and feasibility. The strategy that would best meet all criteria was the jet fan option. The recommended system consists of jet fans in the tunnels generally located 50 meters from each end of the stations. The jet fan operating mode would be dependent on the location of the fire within the station.

CFD ANALYSIS

A CFD analysis was performed using a commercially available CFD software, run on a DEC Alpha workstation. For the last five years, the SES program has been used in conjunction with CFD to simulate fire emergencies in subway stations where three-dimensional modeling is more appropriate. While CFD has the capability to model more complex station geometry, the SES program provides the fundamental boundary conditions necessary for the CFD analysis. This coupling of computer tools has helped subway ventilation engineers to solve problems and analyze situations where conventional techniques would have failed or been grossly inadequate.

CFD simulations were performed to evaluate the station conditions resulting from a fire on board a train stopped in a station with and without mechanical ventilation. For natural ventilation (i.e., no mechanical ventilation), ambient pressure was assumed at all flow boundaries. For mechanical ventilation, simulations were performed to determine the airflow boundary conditions at the ends of the station. Ambient pressure conditions were used at station entrances.

Two stations were selected for the simulations:

Medrano Station is a cut-and-cover station with side platforms and no mezzanine. The station is about 130 m long, 33 m wide, and 6 m high. The station has a total of four exits. Each platform has two exits to outside ambient. Figure 1 shows the general layout of the station. The computational grid used for this station is about 84,000 cells. The grid consists of 117 cells in the longitudinal x-direction, 20 cells in the vertical y-direction, and 36 cells in the lateral z-direction. The number of cells is based on previous project experience with consideration of the accuracy required in the study.

Pueyrredon Station is a bored tunnel station with a mezzanine above the two side platforms. The station is about 130 m long, 21 m wide, and 10 m high. Two escalators and one stairway connect each platform to the mezzanine. This station has five exits. Figure 2 shows the general layout of the station. The computational grid used for this station was about 85,000 cells. The grid consists of 131 cells in the longitudinal x-direction, 21 cells in the vertical y-direction, and 31 cells in the lateral z-direction.

Two fire scenarios were considered: (1) a fire at either end of the station beyond the last exit or staircase and (2) a fire

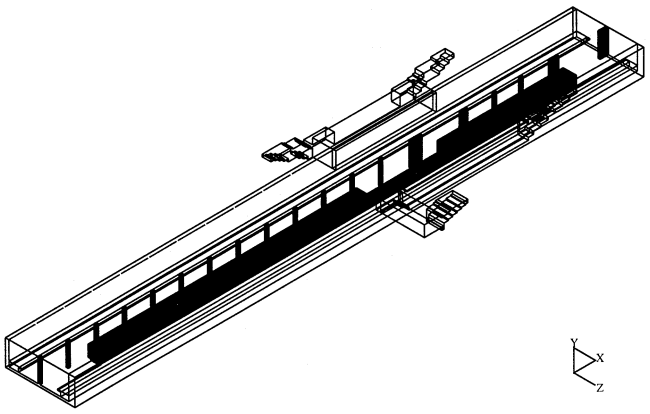

Figure 1 *Medrano station layout. Grid (117 × 20 × 36).*

clustering of the Method 3 curves around the Method 2 curve. Also note the position of the Method 1 curve. For these calculations, the Method 1 curve represents the fastest predicted filling of the atrium volume.

Figure 5 also illustrates the predicted filling rates, but in this instance, smoke densities have been adjusted based on the calculated average plume temperature. Note the shift of the Method 3 curves toward the origin. Note also that Method 1 no longer predicts the fastest filling of the atriums. Tests 4 and 7 now fall closer to the origin than the Method 1 curve. The Method 2 curve now represents nearly the slowest filling rates.

Figure 6 compares the results from the LES CFD simulations to Methods 1 and 2. The LES CFD results are trendlines derived from the raw data observed from the LES CFD simulations (see Table 2 for LES CFD observed data). The LES CFD simulations show the general distribution of the

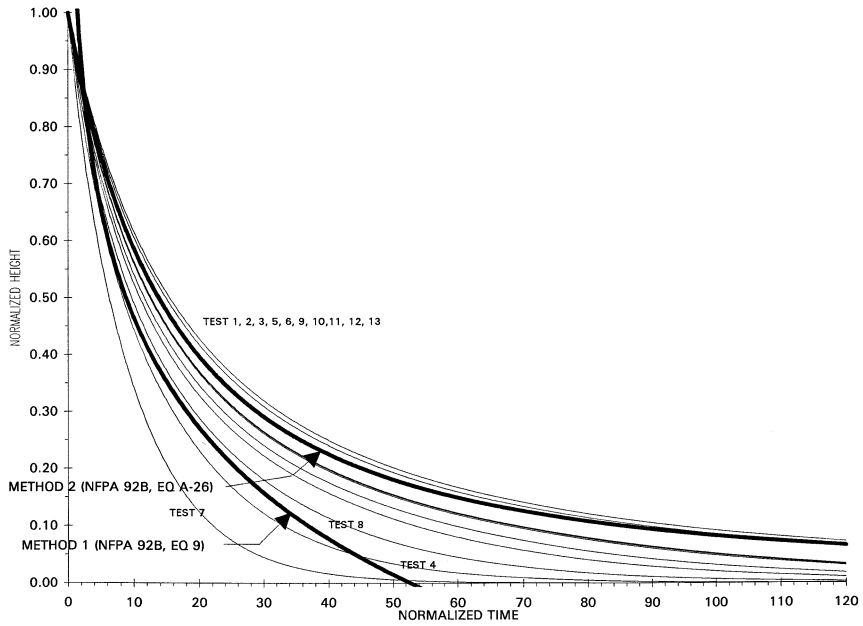

Figure 5 *Calculation methods 1, 2, and 3. (Calculation method 3 adjusted for smoke layer temperature; Method 3 calculations identified by test number.)*

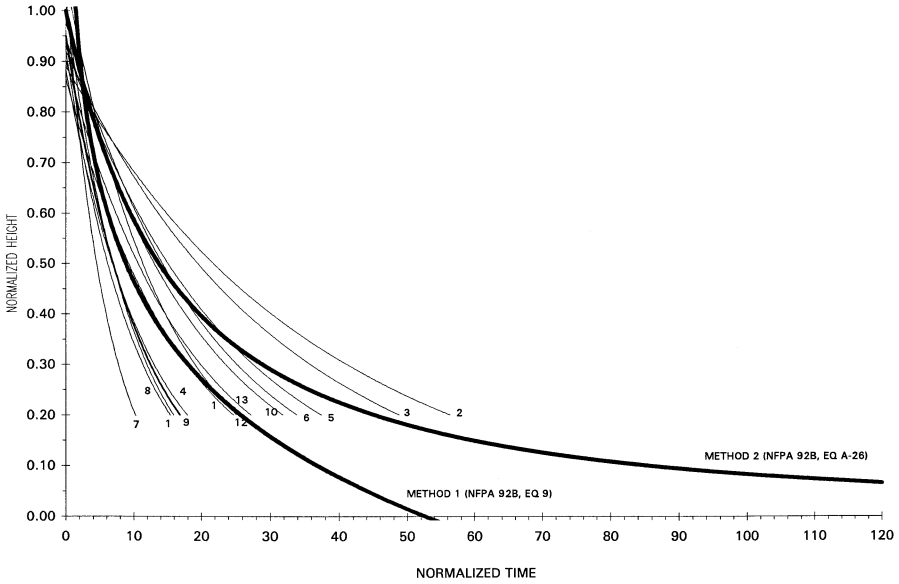

Figure 6 *Calculation methods 1 and 2. (Compared to large eddy simulation CFD predicted curves; LES CFD curves identified by test number.)*

also serves as the heat pump that both entrains air into the active combustion zone and then circulates the combustion products through the surrounding enclosure. It is the latter role that is of interest here. Although the central role of the fire plume has been recognized for some time, there is still much uncertainty about the plume structure. Indeed, Zukoski (1994) gives a recent summary of the state of knowledge of mass entrainment into isolated fire plumes. There is clearly no consensus on any simple formula or graphical correlation for this most basic of plume quantities. Much of this uncertainty arises from the experimental and conceptual difficulty associated with determining the outer plume boundary. McCaffrey (1979) developed centerline mean velocity and temperature correlations that are consistent with a large body of experimental data (Baum and McCaffrey 1989).

To perform a computational study of an isolated fire plume, the minimum length scale that must be resolved is the plume structure scale.

$$D^* = (Q/\rho_0 c_p T_0 \sqrt{g})^{2/5} \tag{15}$$

D^* is roughly comparable to the plume diameter near the base. It involves the heat release rate Q directly and can be seen both in the dimensionless form of McCaffrey's plume correlations and by considering the dimensionless form of the Navier-Stokes equations for this problem. In fact, if the equations discussed above are made nondimensional with D^* as length scale, $\sqrt{gD^*}$ as velocity scale, $\sqrt{(D^*/g)}$ as time scale, and T_0 as temperature, all the physical constants disappear from the inviscid terms in the equations. Only Reynolds and Prandtl numbers appear in the viscous stress and heat conduction terms.

In order to simulate the convective mixing of the fire plume, the grid spacing should be about 0.1 D^* or less. Figure 1 shows an instantaneous snapshot of three temperature contours obtained from a 96 × 96 × 96 cell simulation. The contours correspond to the boundaries of the continuous flame, intermittent flame, and plume zones as defined by Baum and McCaffrey (1989). Note that the image is an instantaneous snapshot of the fire and that time averages of the output of this kind of simulation must be produced in order to make quantitative comparison with most experimental data. Indeed, it is the fact that the results of the simulation can be averaged in a routine way while the equations of fluid mechanics cannot that is the basis of the whole approach presented here.

On the left of Figure 2 are the instantaneous vertical centerline velocity and temperature profiles superimposed on the steady-state correlation of McCaffrey (circles). The oscillations are primarily due to the large toroidal vortices generated at regular intervals at the base of the fire, which then rise asymmetrically. Note that the flow is not even remotely axially symmetric and the centerline is defined only by the geometry of the pool at the base of the plume. The right side of Figure 2 shows the corresponding time-averaged quantities (solid lines) and McCaffrey's centerline correlations. The time-averaged flow is symmetric and in excellent agreement with the correlations. The major deviations are at the bottom of the plume, where the thermal elements are turned on instantaneously without any preheat as they leave the pool surface. Otherwise, the boundaries of the computational domain are open. At these open boundaries, the perturbation pressure is assumed zero. This is a reasonable approximation at the side boundaries but less so at the top. Various strategies have been explored to properly set the conditions at the top, but in most instances, there is usually a solid ceiling or a hood drawing the combustion products up at some specified flow rate. Figure 3 shows the corresponding radial dependence of the vertical velocity and temperature at heights of $z/D^* = 2.8$ (intermittent region) and $z/D^* = 5.3$ (plume region). The results of the simulation are compared with Gaussian profiles that incorporate the half-widths obtained from McCaffrey's correlations.

Figure 1 *Instantaneous snapshot of a pool fire simulation performed on a 96 × 96 × 96 grid. The contours correspond roughly to the boundaries of the continuous flame, intermittent region, and plume. The square burner is of length D* with the height of the computational domain rising to about 12 D*.*

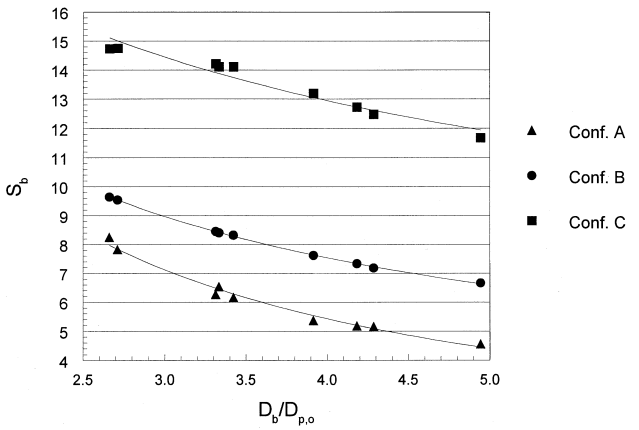

Figure 2 *Borehole shape factor relations for thermal resistance pipe configurations.*

TABLE 1
Curve Fit Coefficients for
Shape Factor Correlation in Equation 3

Configuration	β_0	β_1	Correlation Coefficient
A	20.10	−0.9447	0.9926
B	17.44	−0.6052	0.9997
C	21.91	−0.3796	0.9697

The borehole shape factor data (Figure 2) and the associated curve fit relations (Equation 3 and Table 1) provide a convenient method for calculating effective grout thermal resistance for any bore size, pipe size, grout thermal conductivity, and assumed pipe spacing that are commonly encountered in practice.

Currently, when U-bend heat exchanger loops are installed in boreholes, they are simply weighted and sunk or pushed into the borehole. No control over the pipe spacing in the borehole is available. Therefore, an assumption must be made about the average pipe spacing in the borehole before the effective grout thermal resistance can be estimated. The A configuration is a conservative design assumption and should only be considered when large uncertainties exist in the formation thermal conductivity. The B configuration would be an appropriate design assumption in most situations, as it represents an average spacing along the entire borehole length. This assumption would be most appropriate if reliable information is available on the formation thermal conductivity. Configuration C would never consistently occur in practice and is a risky design assumption that could lead to underdesigned loop lengths. Even with very good formation soil thermal conductivity data, a device to ensure this spacing with a very high level of certainty would be required before this level of performance could be realized.

Borehole thermal resistance can be found knowing that the effective grout thermal resistance and the pipe thermal resistances act in series, as shown in Figure 3. The total pipe resistance is equivalent to the thermal resistance of two individual pipe thermal resistances in parallel. Assuming that the fluid temperatures in each pipe are the same, the equation to calculate the equivalent thermal resistance of two pipes in parallel follows:

$$R_{pp} = \frac{R_{p1}R_{p2}}{R_{p1} + R_{p2}} \tag{4}$$

Since the two pipe resistances are equal ($R_{p1} = R_{p2} = R_{pipe}$), Equation 4 reduces to

$$R_{pp} = \frac{R_{pipe}}{2}. \tag{5}$$

Then, the borehole resistance (excluding convection resistance on the inside pipe wall) can be found by adding the effective grout thermal resistance to the parallel pipe thermal resistance:

$$R_b = R_{pp} + R_g. \tag{6}$$

Pipe thermal resistances and parallel pipe thermal resistances for common pipe diameters and dimension ratios used for vertical heat exchanger U-bends are provided in Table 2 (IGSHPA 1988).

Field Tests

The thermal responses of various boreholes with different diameters, depths, pipe sizes, and grout types were measured by Austin (1998), Smith (1997), and Remund (1997). The procedure consisted of rejecting a known rate of heat into the

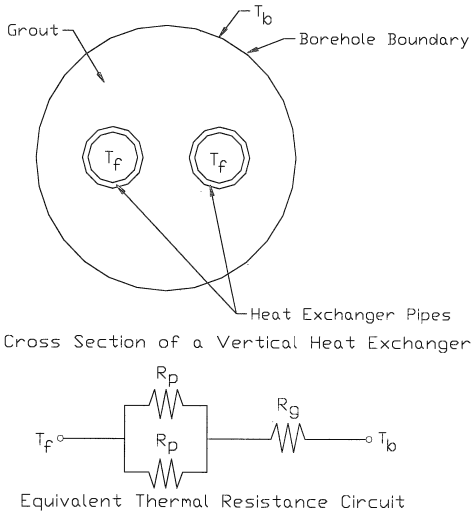

Figure 3 *Parallel-series model for pipe thermal resistance and effective grout thermal resistance.*

Testing of Thermally Enhanced Cement Ground Heat Exchanger Grouts

Stephen P. Kavanaugh, Ph.D. **Marita L. Allan, Ph.D.**
Member ASHRAE

ABSTRACT

Optimal performance of closed-loop, ground-source heat pumps (ground-coupled heat pumps) is dependent upon the thermal properties of the backfill in the annular region between the ground heat exchanger (GHEX) tubes and the outer bore wall. Equally important is the protection of groundwater aquifers from contaminants that may flow from the surface or other aquifers through poorly sealed boreholes. Conventional cement and bentonite-based grouts have relatively low thermal conductivities. Loop requirements often increase beyond the allotted budget in applications where regulatory bodies require the entire heat exchanger length to be grouted.

This paper reports on the results of four mixes of thermally enhanced cementitious grouts. Four grouts were evaluated in a test stand to minimize the impact of external factors typically present in field tests. The test stand accepts up to 6 in. (15 cm) ground heat exchangers in a 10 ft (3 m) test section. Controlled testing is performed in either the cooling mode (loop above 85°F [29°C]) or heating mode (loop at 32°F [0°C]), and the temperature of the outer bore wall is held constant with a groundwater source.

Results indicate cement grouts that are enhanced with low-cost additives have thermal conductivities three to four times as large as conventional high-solids bentonite grouts. This would result in reduced heat exchanger lengths compared to those grouted with bentonite. There appears to be no measurable increase in overall borehole resistance due to separation of the colder tubes from the grout in the heating mode. This discussion does not include pumpability, permeability, and material handling issues, which must be thoroughly investigated before any grout can be recommended for use.

INTRODUCTION

The vertical ground heat exchanger (GHEX) is an important component in a ground-coupled heat pump (GCHP) system. The design must balance the constraints of high thermal performance, reasonable cost, durability, and ease of installation. An additional constraint must be imposed in order to ensure that these systems maintain their positive environmental advantage. This requirement is to prevent contaminated surface water or water from a poor quality aquifer from entering into drinking water or irrigation aquifers.

Figure 1 demonstrates the components of three situations encountered in the installation of vertical U-tube GHEXs. A 3.5 in. to 6 in. (9 cm to 15 cm) diameter bore is drilled in the

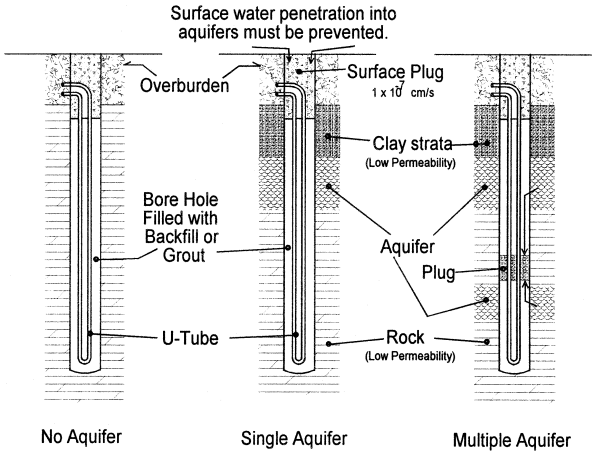

Figure 1 *Hydrogeological variations for GCHP U-tube heat exchangers.*

Stephen P. Kavanaugh is a professor of mechanical engineering at the University of Alabama, Tuscaloosa. **Marita L. Allan** is a scientist at Brookhaven National Laboratory, Upton, N.Y.

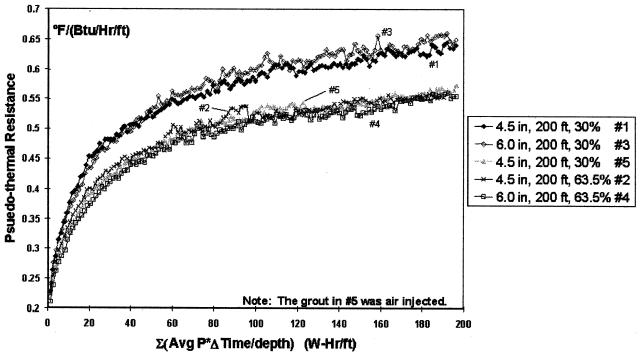

Figure 4 *Pseudo-thermal resistance as a function of cumulative power per depth of loop, Brookings, South Dakota.*

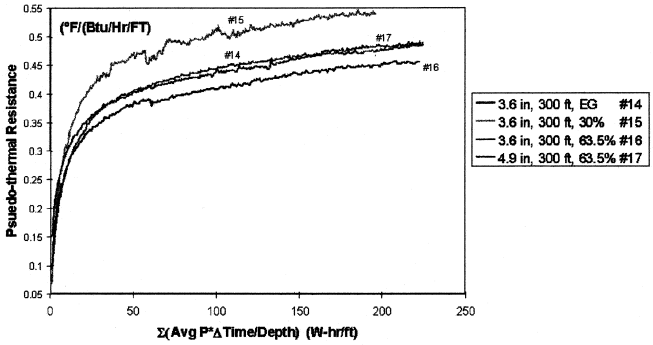

Figure 5 *Pseudo-thermal resistance as a function of cumulative power per depth of loop at a convenience store in Bartlesville, Oklahoma.*

bore) to some extent, which has the effect of enhancing the borehole thermal conductivity. This feature is considered to be the primary reason for the higher performance.

According to theory, borehole 1 should have a lower pseudo-resistance profile than borehole 3 because the same grout was used in a 4.5 in. (0.114 m) borehole as in a 6 in. (0.152 m) one. Use of the thermal resistance method, shown in Figure 4, produces the results expected. Although the two curves for boreholes 1 and 3 in Figure 4 are not separated by a large amount, they are distinctly separate, and the greater the difference between the formation thermal conductivity and the grout thermal conductivity, the greater the difference would be between curves such as no. 1 and no. 3.

The curves shown in Figure 4 for boreholes 2 and 4 converge. Temperature and time at this site were used to determine the average thermal conductivity of the formation from the five boreholes and resulted in a value of 1.079 Btu/ft·h·°F (1.867 W/m·°C); the measured grout thermal conductivity used in boreholes 2 and 4 is 0.85 Btu/ft·h·°F (1.471 W/m·°C). Since the grout and formation thermal conductivity are close to the same, it is expected that borehole diameter would not significantly change the thermal resistance values. This is apparent when noting that borehole 2 is 4.5 in. (0.114 m) in diameter and borehole 4 is 6 in. (0.152 m) in diameter, but the curves in Figure 4 are essentially the same. The relative positions of the curves in Figure 4 demonstrate that enhanced grout performs significantly better than standard bentonite grout.

CHARACTERISTICS OF BARTLESVILLE, OKLAHOMA, TEST BOREHOLES

Seventeen boreholes were drilled in a single field to provide energy for a convenience store in Bartlesville, Oklahoma. DOE provided funding to complete and evaluate the performance of the last four. These are in a line at the end of the field of heat exchanger loops. Boreholes 16 and 17 were completed with 63.5% solids-enhanced grout, the same as in test sites described previously. Borehole 15 was completed with 30% solids bentonite grout, which was used at two of the previously described sites. Boreholes 1 through 14 were completed with a native Oklahoma sand-bentonite mix (native EG) with a portion of cement added. This was the first time that a bulk mixture of this type was tested for field performance.

The distribution of the curves (Figure 5) among boreholes 15, 16, and 17 is as expected from a theoretical viewpoint. Borehole 15 is bentonite-grouted and of the same diameter as all the others except no. 17, which is a 4 7/8 in. (0.124 m) borehole. Because the grout thermal conductivity in borehole 15 is lower, the pseudo-thermal resistance, as shown in Figure 5, is highest. Borehole 17 contains enhanced grout, but the borehole diameter is greater, so the pseudo-thermal resistance would be expected to be lower than that of holes filled with bentonite. Borehole 16, with 63.5% solids-enhanced grout and a smaller borehole, would provide a lower thermal resistance, as indicated in Figure 5. Because grout in borehole 14 is enhanced with sand, the pseudo-thermal resistance was expected to be lower than that of the bentonite-grouted borehole 15; however, its relation to the 63.5% solids-enhanced grout was not predicted. Figure 5 shows that native Oklahoma enhanced grout performs in essentially the same manner in a 3 5/8 in. (0.092 m) borehole as 63.5% solids-enhanced grout performs in a 4 7/8 in. (0.124 m) borehole. Since the larger borehole degrades the performance but the 63.5% solids grout performs the same as the EG-enhanced grout, then the conclusion is that the 63.5% solids grout performs better than the EG-enhanced grout.

Contrary to results of the South Dakota tests, comparison of effects of enhanced grout with changes in borehole diameter at Bartlesville shows a distinct difference between the two 63.5% solids grout tests. The following hypothesis was verified by tests of the two 63.5% solids-enhanced grouts: where conductivities of grout are close to the formations' thermal conductivities, borehole diameters will have no effect; where a difference exists in the thermal conductivities, performance degradation occurs as the borehole gets larger. Tests on the four Bartlesville bores produced an average formation thermal conductivity of 1.68 Btu/ft·h·°F (2.907 W/m·°C), which is almost twice the thermal conductivity of the grout—thus the

TABLE 1
Physical Properties of the Test Oils

Type	Viscosity (SUS/100°F)	Viscosity (cSt/100°F)	Pour (°F)	Pour (°F)	Specific Gravity	Surface Tension (dynes/cm)
3GS	155	33	−40	−65	0.91	47
5GS	525	113.4	−10	—	0.918	40

refrigerant used in the this study is R-22, whose thermodynamic and transport properties were evaluated using the computer program REFPROP (NIST 1997).

EXPERIMENTAL PROCEDURES

Initially, the test section was cleaned and checked for leakage before it was evacuated. Then the system was evacuated using a turbo-molecular vacuum pump. The vacuum pump continued working for another two hours after the vacuum gauge manometer reached 10^{-4} torr to ensure that it contained no noncondensable gases. Before obtaining a series of experimental data for the boiling of mixtures with different compositions, the experimental setup was cleaned thoroughly prior to filling the vessel with the refrigerant. Pool boiling experiments were conducted at saturation temperatures of −5°C, 4.4°C, and 20°C. The liquid refrigerant mixture was gradually preheated to its corresponding saturated state before running each test. Power was then adjusted to a predetermined value. The criteria for the steady-state condition were variation of system pressure to be within ±3 kPa and mean temperature variations of the wall surface less than ±0.1°C over five minutes. All the data signals are collected and converted by a data acquisition system (a hybrid recorder). The data acquisition system then transmits the converted signals through GPIB interface to the host computer for further operation. The experimental uncertainties reported in the present investigation were analyzed following the single-sample method proposed by Moffat (1989). The maximum and minimum uncertainties of the heat transfer coefficients were estimated to be approximately 18.4% for $\dot{Q}$ = 3 W and 3.5% for $\dot{Q}$ = 700 W.

DATA REDUCTION

The heat transfer coefficient for each power input was calculated as follows:

$$h = \frac{\dot{Q}}{A_{wall}(T_{wall} - T_s)} \tag{1}$$

where $\dot{Q}$ is the electric heating power and T_s is the saturation temperature for pure refrigerant based on the measured system pressure. The outside surface area, A_{wall}, is evaluated as $\pi D_o l$. Note that D_o is the outside tube diameter, and l is the effective length of the cartridge heater (the length of the cartridge heater is 100 mm). T_{wall} is the mean average wall temperature at the outer surface, which can be calculated from the measurement of inside temperatures and is given by

$$T_{wall} = T_{wi} - \dot{Q}\frac{\ln(D_o/D_i)}{2\pi k_w l} \tag{2}$$

where T_{wi} is the arithmetic mean of three inside wall temperatures:

$$T_{wi} = \frac{T_{w1} + T_{w2} + T_{w3} + T_{w4}}{4} \tag{3}$$

where T_{w1}, T_{w2}, T_{w3}, and T_{w4} are the inside wall temperature readings.

EXPERIMENTAL RESULTS

Figure 3 shows a comparison of heat transfer coefficients and the predictions by the correlations from Cooper (1984) and Gorenflo (1993). As seen, the predictions by the

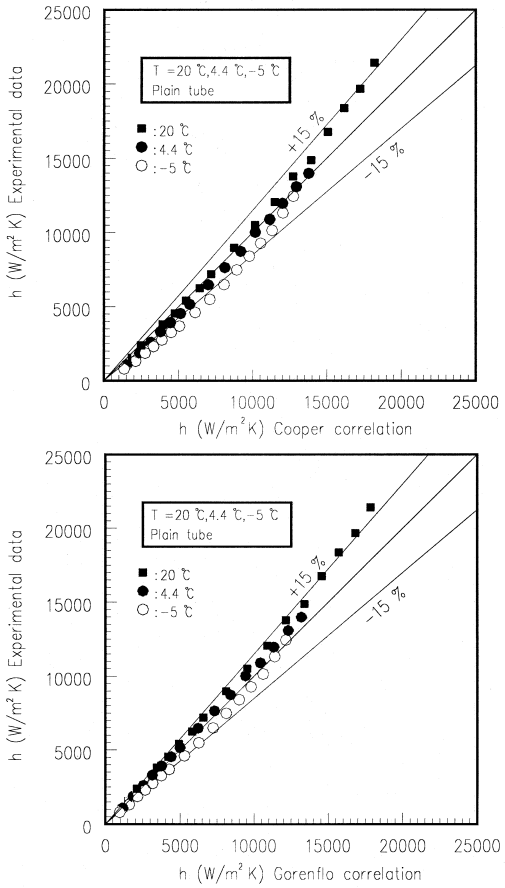

Figure 3 *Comparison of the R-22 plain tube data with correlations.*

cial flooded evaporator units. Saturation temperatures of 40°F and 80°F (4.4°C and 26.7°C) were used.

The presence of oil in a tube bundle has a significant effect on the boiling process for both plain and finned tubing. With smooth brass tubes in a bundle, Cotchin and Boyd (1992) utilized R-113 with and without oil in a 60-row by 3-column bundle section. Electric cartridge heaters provided the heat load and a pump circulated the refrigerant across 1 in. (25.4 mm) tubes. It was found that up to 20%, by volume, oil concentration could increase the heat transfer. Using R-12, Danilova and Dyundin (1972) examined finned copper tubes in six rows. Negative performance effects are noted with 8% oil, by weight. The oil contamination reduced boiling coefficients by 5% to 50%, depending on saturation temperature and heat flux, and had the greatest impact at the lower heat fluxes. Likewise, tube row performance variation is more pronounced with oil in the bundle.

Memory et al. (1995) examined R-114 and R-114/oil pool boiling using smooth, 19 fpi (Gewa-K), turbo-B, and high-flux surfaces. As expected, average bundle coefficients improved with oil content up to about 3% with the smooth and finned tube types. Between 4% and 10%, the coefficients decreased somewhat; in all cases, there was improvement over the no-oil case. The oil enhancement ranged from 20% to 60% over that of the pure R-114 fluid with the finned tubes; the plain, smooth tube case showed improvement of 20% to 40%.

Given the limited available information in the open literature in conjunction with the use of alternative refrigerants, it becomes necessary to provide added data, particularly for other refrigerants flow boiling in finned tube bundles. Thus, the focus of this study is the experimental determination of the effects of oil on heat transfer with R-123 and R-134a with this type of tube.

REFRIGERANT FLOW LOOP

The experimental setup is displayed, in schematic form, in Figure 1. It consists of a tube bundle test section, in which the refrigerant boiling takes place, within a pressure test chamber. The vapor refrigerant out of the tube bundle test section is condensed by the two lower coils arranged in parallel and by the presence of a third cooling coil located above the test section, inside the test chamber. This heat is ultimately rejected by a nominal ten-ton, air-cooled external chiller that circulates a 40% (by weight) ethylene glycol/water solution through the condenser coils. The chilled water solution ranges from 15°F to 25°F (–9°C to –4°C) depending on the total rate of heat rejection in the test section. From the lower condensers, the liquid is pumped through a bank of rotameters so that the flow rate can be measured. Liquid refrigerant can be directed to any of four rotameters having capacities ranging from 3.67 gpm to 0.2675 gpm (13.89 L/min to 1.01 L/min) of water. The choice of rotameter is based upon the refrigerant mass flow rate to ensure mid-scale readings. The liquid stream is then passed through the in-line electric heater piping section to generate the appropriate amount of vapor (15% inlet vapor quality).

The heater is located in the liquid refrigerant line between the rotameters and test section inlet. To prevent separation of any oil from the two-phase refrigerant mixture, the heater piping is sloped upward so that the oil, vapor, and liquid remain well mixed and are carried to the test section. (Other types of separate boiler facilities would serve to concentrate the oil inside the facility, over time, as the vapor is produced.) The two-phase flow crosses a distributor plate and then passes upward, through the tube bundle in the test section, perpendicular to the axis of the tubes. Heat from the tube bundle converts the two-phase mixture to vapor that exits the top of

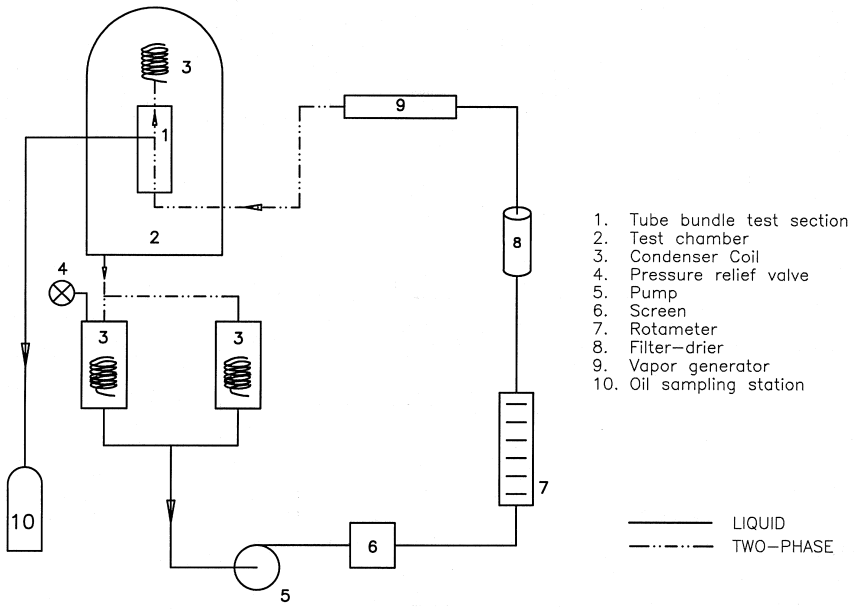

Figure 1 *Flow boiling test loop.*

h_o is found. At higher oil content, the difference between the top and middle tubes and the bottom tube is magnified; the coefficient can be three times greater for the upper tubes, as seen in Figures 12 and 13. Except for the bottom tube, at higher oil concentrations the heat transfer is relatively insensitive to heat flux, even decreasing slightly with q_o.

Overall average oil effects are noted in Figure 14. The heat transfer is typically increased, based upon the pure R-134a boiling reference. At 1% oil, the results are mixed, with a slight decrease at low q_o and a small increase for q_o > 5200 Btu/h·ft^2 (16,404 W/m^2). In the 2% to 7% oil range, h_o can be 30% to 70% larger, 50% being typical, than the no-oil case. At higher oil content, the heat transfer advantage appears to level off and may begin to reduce near 10% oil. Table 2 contains all of the oil-related data for the R-134a. (Again, the location of each oil port is found in Figure 2.)

R-22 Data Trends

Figure 15 presents the R-22 experiments. Only pure R-22 was tested in the bundle after the R-134a. Qualitatively, the

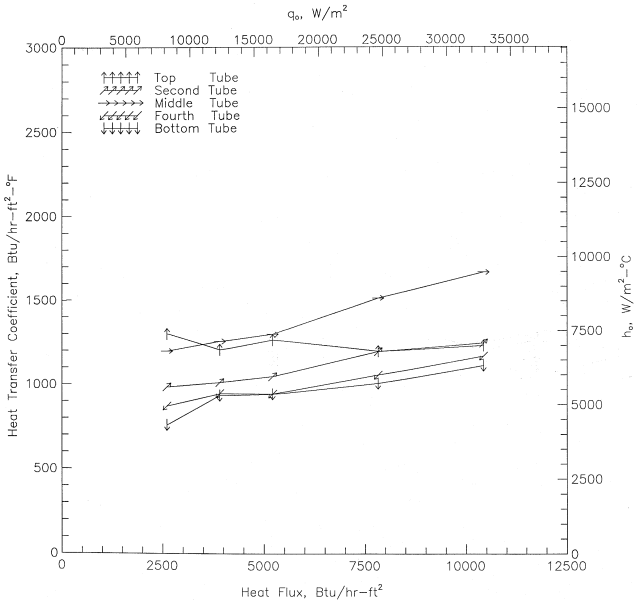

Figure 10 *Individual 26-FPI/R-134a tube performance with 0% oil.*

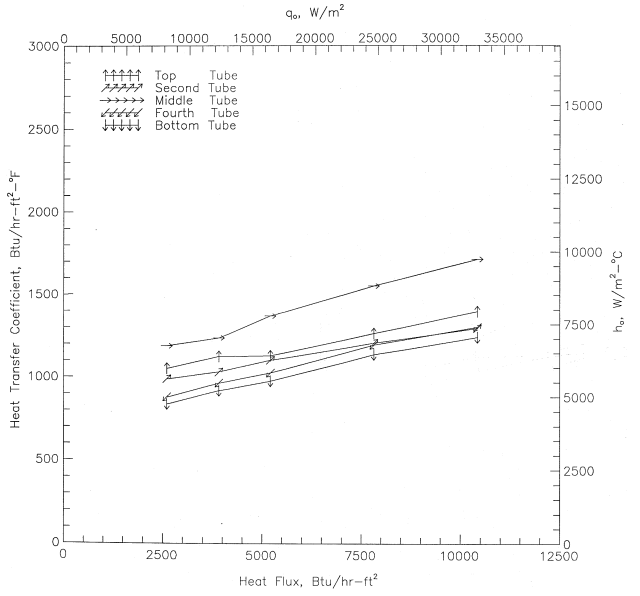

Figure 11 *Individual 26-FPI/R-134a tube performance with 4% average oil.*

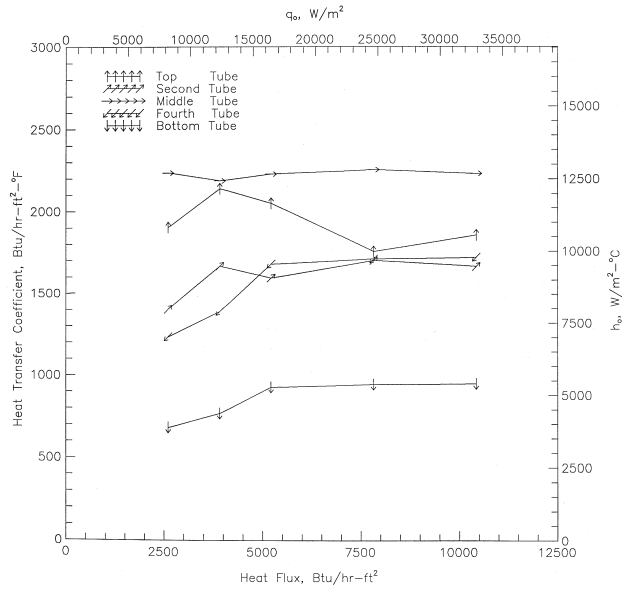

Figure 12 *Individual 26-FPI/R-134a tube performance with 1% average oil.*

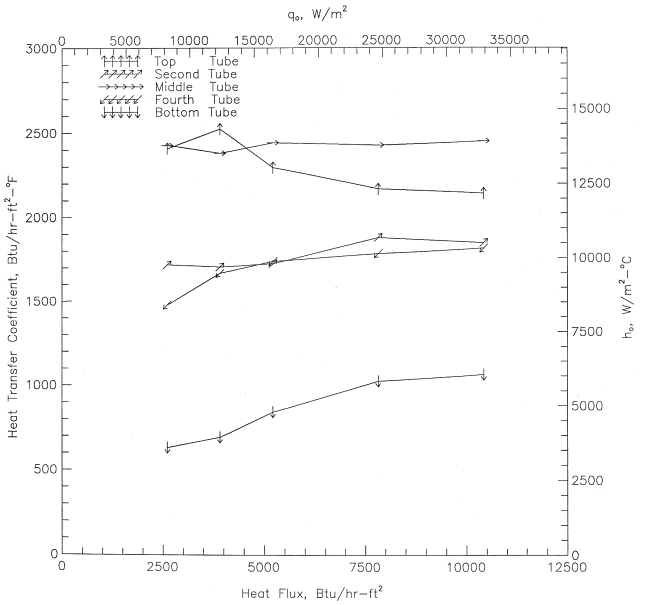

Figure 13 *Individual 26-FPI/R-134a tube performance with 6% average oil.*

despite improvements in technology, this remains quite a challenge.

Interactions between air conditioning and refrigerated cases influences energy consumption and sales parameters (food integrity and appearance, thermal discomfort). Besides thermal coupling, air carried in through front doors and customer traffic is also a source of moisture. Display cases continuously operate as heat and moisture traps. Because the freezer case (see Figure 3) evaporation temperature is near −35°C (−31°F) (vs. about 4°C [39°F] for a rooftop air conditioner), when cases cool the indoors, it is energy consuming. Furthermore, dehumidification in display cases is inefficient due to the additional energy required for defrosting and re-cooling cycles. The aim is to develop a new approach to study this interaction and to look for an optimal indoor air condition, using real figures.

Literature Review

Although supermarket energy challenges are well set in Adams (1985), the interactions between refrigeration and air conditioning are often unknown or misunderstood. The traditional separation of the air-conditioning and refrigeration industries has limited exchange of design information. Nevertheless, since the early 1980s, some progress has been made. For example, the development of efficient desiccant cooling in the United States is described in Meckler (1992). The air in the entire supermarket is maintained at a low humidity. In France, another type of humidity control is currently being tested, which consists of supplying a very dry air curtain just behind the display case (Bernet 1997).

Energy analysis is developed in Khattar et al. (1991) using the TRNSYS building simulation model. However, this study is mostly based on detailed modeling of various refrigeration components and on possible improvements of the refrigerating system. It gives no evidence of the interaction between air conditioning and refrigerated cases. A significant work on the influence of indoor humidity on refrigerated display case consumption is presented in Howell (1993a). It considers two types of air curtains according to display case types (horizontal or vertical) in order to calculate heat and moisture exchanges. The results are validated by experimental data. In Howell (1993b), regression equations are used to evaluate heat and moisture transfers under any indoor relative humidity for typical cases. Building simulation was used to see the influence of the relative humidity control on air-conditioning consumption. Some typical ratios are given for a warm and humid climate (Tampa, Florida) in Howell et al. (1997): a 5% reduction in store relative humidity gives a total store energy load reduction of nearly 5%. However, indoor temperature set-point influence was not studied in this paper. Another point is that supermarket dimensions in the United States are very different from those in France, which influenced the decision to make some appropriate simulations.

No modeling of the cold aisle phenomenon, which is essential in the analysis of coupling, has been found. If one were to set display case operation to indoor conditions equal to those found in the other sales areas, there could be large mistakes in global energy consumption calculations. In Orphelin et al. (1997), the authors have proposed an approach to this problem, and a more complete sensibility analysis is proposed in Orphelin and Marchio (1997). The main points of this methodology are given in this paper. The analysis here is focused on indoor humidity set-point influence on energy consumption.

EQUIPMENT MODELING

Figure 1 shows the considered points—outside, indoor, supply, cold aisle, positive case, and negative case—defined at each time interval by (*T*; RH). When considering display cases, one has to distinguish between refrigerator cases, which operate at *D*+ (2°C to 4°C [36°F to 39°F]; 70% to 80% RH), and freezer cases, which operate at *D*– (–20°C to –18°C [–4°F to 0°F]; 80% to 90% RH). Before studying the interaction between air conditioning and display cases, the models for each of these systems are proposed separately.

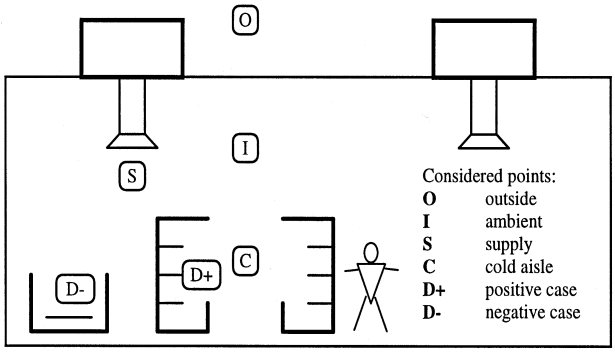

Figure 1 *Cross section of a supermarket.*

Rooftop Air Conditioners

Air-conditioning systems are sized to operate at a maximal thermal load, corresponding to the nominal operation. However, the system always works under different conditions and mostly under partial loads (60% to 90%). Consequently, valid electric consumption calculations have to be made with a part-load rooftop air-conditioner model. Some models exist but generally require much information, which is often unavailable. A simplified model of a rooftop air conditioner described in Stan (1995) is used in this study. If P_E is the effective power input and P_C is the cooling energy rate, then the ratio P_E/P_C is approximated as a second-degree polynomial, as explained in more detail in Stan (1995):

$$\left(\frac{P_E}{P_C}\right) = \left(\frac{P_E}{P_C}\right)_{nom} \cdot \left(C_1 + C_2 \cdot \Delta T + C_3 \cdot \Delta T^2\right) \quad (1)$$

where

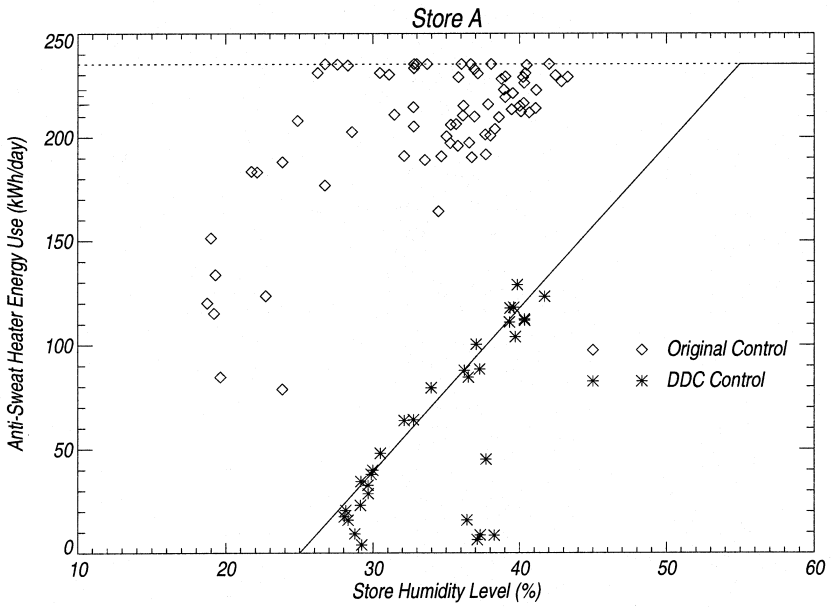

Figure 6 *Anti-sweat heater energy use trend with space humidity at Store A.*

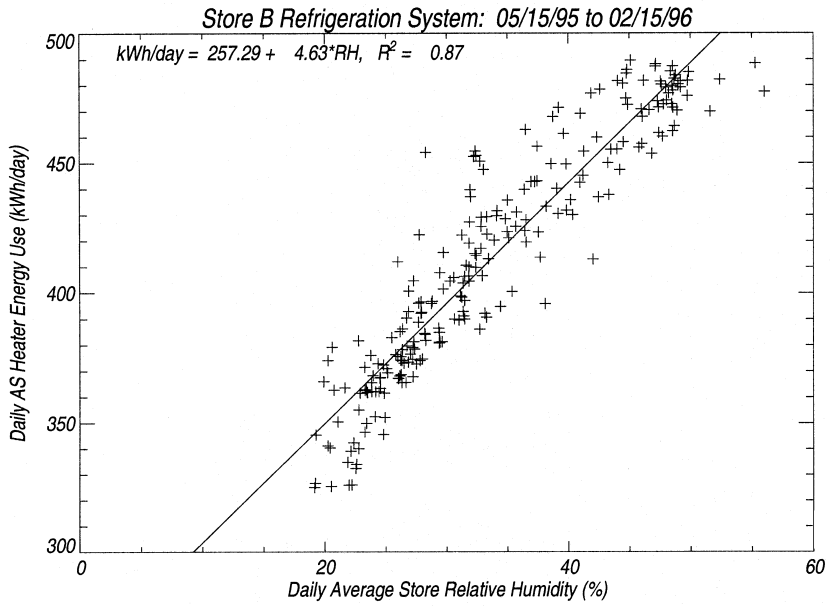

Figure 7 *Anti-sweat heater energy use trend with space humidity at Store B.*

TABLE 4
Reduction in Anti-Sweat Heater Energy Use per Percent Drop in Space Humidity

Reduction per Each % RH Drop in Space Humidity	Store A		Store B	
	(kWh/day per %RH)	(% per %RH)	(kWh/day per %RH)	(% per %RH)
Mechanical Controls	3.5	1.5	4.6	2.1
DDC Controls	7.8	3.3	–	–

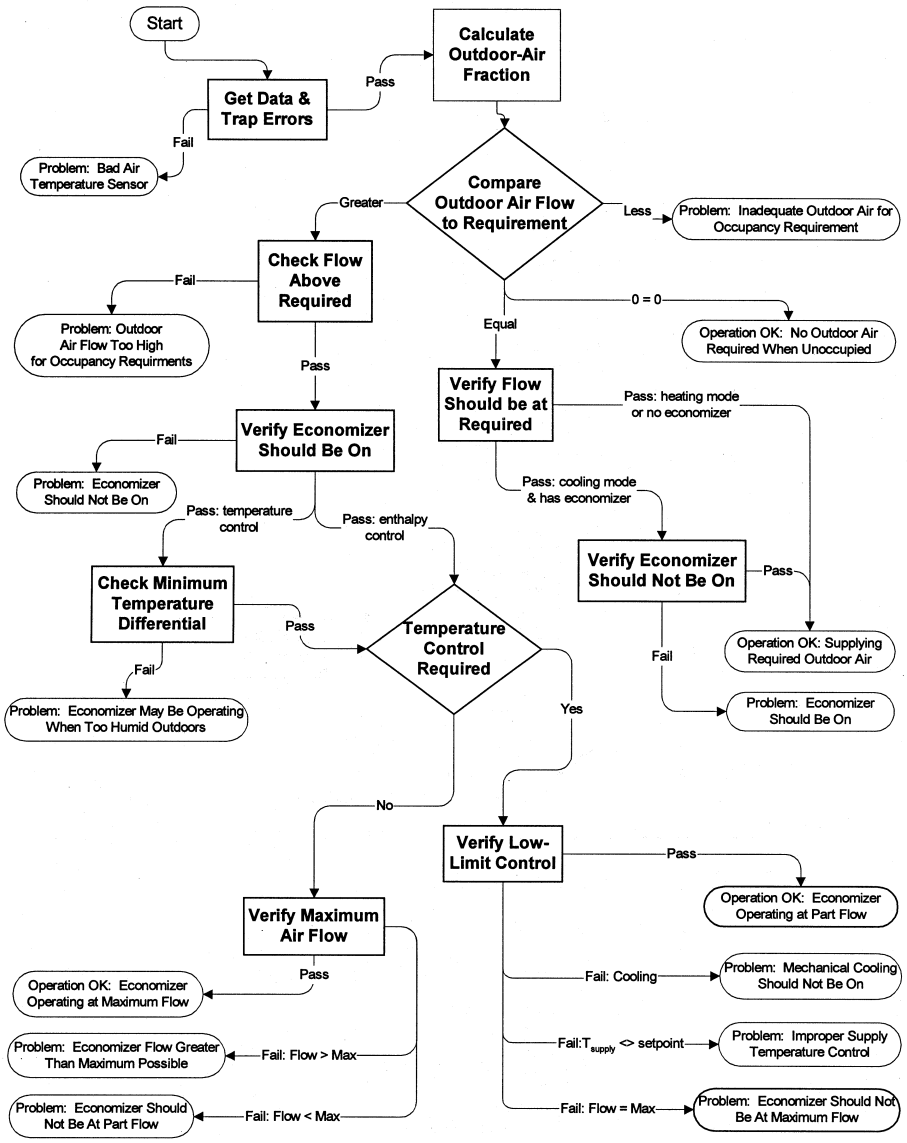

Figure 1 *Overview of the diagnostic logic tree, showing key operating states.*

could be collected using custom metering and data collection systems, or the diagnostician could be used to process an existing database containing the required data. The setup data, obtained by querying the user (building operator or installer), includes information describing the type of economizer, its control strategies and set points, and building occupancy (and hence, ventilation) schedules.

DIAGNOSTIC SOFTWARE

Software Architecture

The OAE Diagnostician is implemented as a module of the Whole-Building Diagnostician (WBD). The WBD is a modular diagnostic software system (see Figure 2) that provides detection and diagnosis of common problems associated with HVAC equipment and lighting in buildings. Modules within the WBD will provide specific collections of these diagnostic functions. The OAE, as one of those modules, monitors, detects, and diagnoses problems with outdoor-air ventilation and economizer operation.

The WBD is implemented on a desktop computer. The diagnostic modules use a central database and share a common graphical user interface. Typically, the user interacts with the WBD to start analysis or to view results of diagnoses. Data are stored in the database by an external process. The data may originate directly from a BAS or other data acquisition system or may already be stored in another database. Diagnostic modules access the central database to obtain configuration data and measured data to be analyzed and to store the diagnostic results. Diagnostic modules can process (i.e., analyze) the information as it is stored or batch-process time-series data or entire databases. The user may schedule processing at regu-

Diagnostics become highly inaccurate when different or multiple concurrent faults produce very similar patterns. In most cases, faults and their symptoms are nested, i.e., one fault may have many symptoms and one symptom may be associated with many faults. For example, the occupants report that the room temperature is too high. This is a symptom. We can easily give many possible faults that could cause this symptom, such as the thermostat in the room is out of order, or the reheat coil valve in the VAV box is stuck open, or maybe the actuator of the cooling valve doesn't work anymore. That's not all. In more complicated situations, several faults may happen simultaneously. Different control loops in the HVAC system may be chained together; one could affect another. An abnormal control loop could cause faults in other control loops, and they may finally form a cycle that makes it harder to determine which one is the original or the primary source of fault.

The objective of this paper is to apply different methods and technologies to on-line monitoring of HVAC system performance, detection of abnormalities, and diagnosis of system faults. The next sections will present (1) the generation of a three-tier system model based on system components and system behavior, (2) the representation of useful knowledge for real-time system monitoring and FDD, (3) the system architecture and the FDD system model with the implementation schemes used in data collection, data processing, and data analysis, and (4) results and discussion.

HVAC SYSTEM MODELS

Modeling accuracy is dependent on the depth of knowledge captured in the model, the accuracy of the basic structure, the function, and the behavior of objects included in each class. Ideally, to build accurate HVAC system models in fault detection and analysis, information captured from the product data models used in the design stage of the new system, such as fan data, ductwork design, shop and as-built drawings, coil design, and manufacturers' specification data, are all needed to both define static attributes and represent the dynamic behavior of the entire HVAC system. Furthermore, field measurements and test data defining actual system capacities and system response times from the commissioning and application stages must also go into any useful model.

The information contained in the models must be based on all of the various sources of knowledge within the HVAC industry, such as

- system design intent and overall mechanical/electrical specifications as well as all component specifications;
- actual installed components, configurations, and specific equipment engineering data;
- test and balance measurements as well as commissioning performance data;
- real-time operating data;
- actual HVAC system digital controller source code as well as sequence of operations;
- day-to-day maintenance information, i.e., repairs, replacements, and adjustments both to physical components, programs, and parameters such as gain, set points, etc.;
- day-to-day input from maintenance and system operating personnel.

To be practical, generic models need to define the underlying behaviors of a class of similar equipment. As each system configuration may change from building to building, libraries of standardized interoperable models should be made available. These models must be then customizable and adaptable to various HVAC system types and to each part.

In this research we propose a three-layer model: system/process/component (Xiao and Han 1998). The *system layer* is an overall envelope that encapsulates the entire HVAC system. For different designs, capacities, and sequences, the system layer decides which process is included, and all the processes together decide the behavior of the entire HVAC system. The *process layer* includes all the processes found in typical variable-air-volume HVAC systems. A typical VAV HVAC system is shown in Figure 1. There are numerous

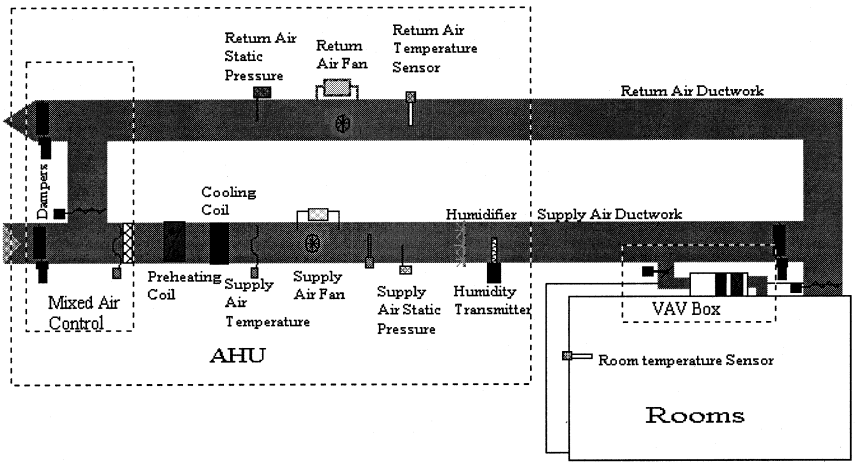

Figure 1 *A typical HVAC system.*

2. Motor control center electricity (2619 complete hourly records)
3. Whole-building thermal energy use (3966 complete hourly records)
4. Whole-building cooling energy use (3964 complete hourly records)

The data set containing these variables has 7944 hourly records in all, but the number of data is less than the number of hours in the pre-retrofit period because records with one or more missing variables were omitted from the training data.

Data for the engineering center are available for both the pre-retrofit and post-retrofit periods. However, there are intervals of missing data in both periods. In this section, three energy end-uses are considered: whole-building electricity, cooling energy, and heating energy. Whole-building electricity is measured in kWh/h and comprises HVAC electrical energy, lights, equipment, and the supercomputer laboratory. Heating and cooling energy are measured in units of MMBtu/h. Neural network models for predicting the use of whole-building electric, heating, and cooling energy were trained on the pre-retrofit data, and then the results shown in this section were generated using the post-retrofit data.

As shown in Table 3, a very dramatic decrease in heating energy occurred after the HVAC system was modified. A substantial decrease in cooling energy use also occurred. Although the whole-building electrical energy use includes some uses that were not subject to the modification of the HVAC system, the whole-building electrical energy also decreased somewhat. The figures noted in Table 3 agree broadly with corresponding results given by Haberl and Thamilseran (1996).

Let us now consider some of the results given by the WBE in a little more detail. Figure 5 shows the computed ECI of whole-building electric energy use for the engineering center during 1992. The computed ECI, as defined by Equation 1, is the actual daily energy use divided by the estimated daily energy use. Note that over most of the year, the computed ECI is in the range 0.6 to 0.9, but toward the end of the year, the ECI increased dramatically. This increased energy use is due to severe cold weather, which caused heating pipes to freeze; to compensate, electrical energy was used for heating instead.

Figure 6 is a detail of Figure 5 showing ECI values during a typical month, September 1992. Note the weekly cycle of values and a general downward trend.

Figure 7 shows the probability of ECI "lower than normal" during September 1992. Note that the increased probabilities correspond to days when the computed ECI was substantially lower than 0.875, as shown in Figure 6. When the computed ECI is only a little lower than 0.875, the probability of "lower than normal" ECI decreases. Also see Figure 4.

As a result of this ECI behavior, the WBE generates a message:

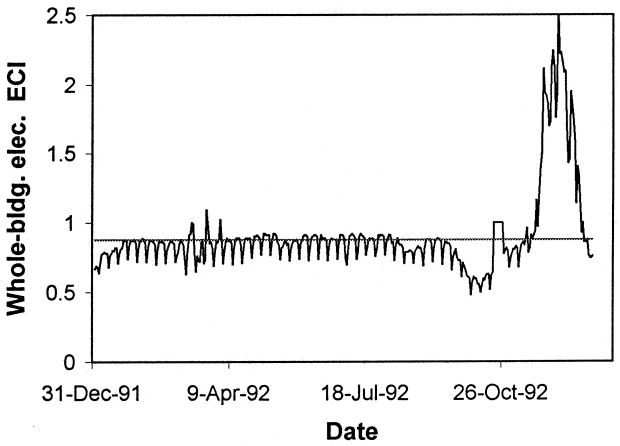

Figure 5 *Computed ECI for whole-building electric energy use in the engineering center in 1992. The horizontal line at ECI = 0.875 marks the upper limit of "lower than normal" ECI values. See the text for a discussion of the marked peak toward the end of the year.*

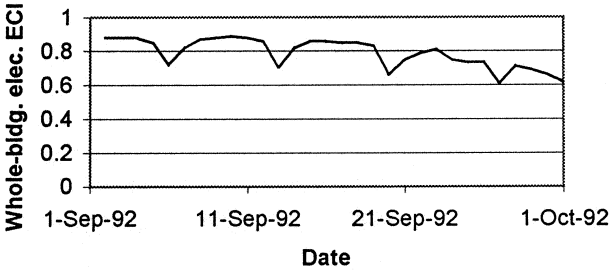

Figure 6 *Whole-building electric ECI values during the month of September 1992. Compare this to Figure 7.*

"*Daily whole-building electrical energy use is significantly lower than normal.*"

This message is generated on each day of the month except for September 1 through September 3 and September 8 through September 10. From Figure 7, it can be seen that those are the days on which the probability of ECI "lower than normal" is relatively small.

Finally, let us consider the total energy savings of the engineering center for the year 1992, as shown in Table 3. We have assumed the same energy costs for the engineering center as Haberl and Thamilseran (1996), namely, $0.0278 per kWh for electricity, $4.67/MMBtu for cooling energy, and $4.75/MMBtu for heating energy. The "Annual ECI" values listed in this table are just the total annual actual energy uses divided by the total estimated energy uses. The heating energy use shows the greatest reduction, while cooling and whole-building electrical use also shows substantial reductions. One would suppose, then, that the HVAC modifications were a success, although the cost of the modifications was not reported.

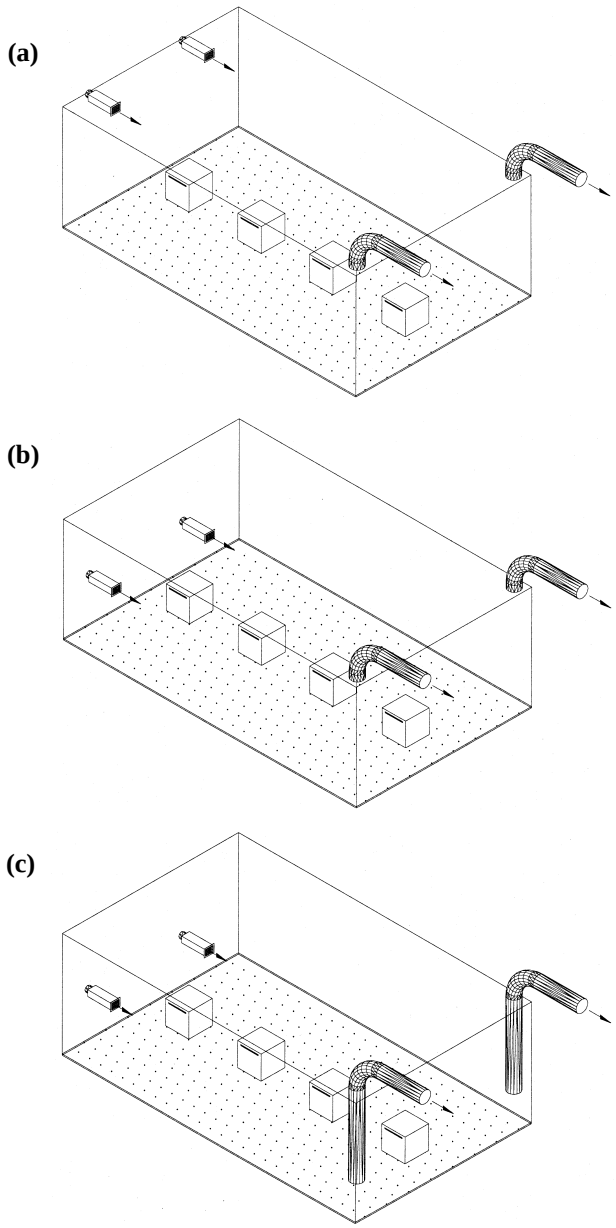

Figure 1 *Single wall configuration. (a) Single wall grille, high-high; (b) single wall grille, low-high; (c) single wall grille, low-low.*

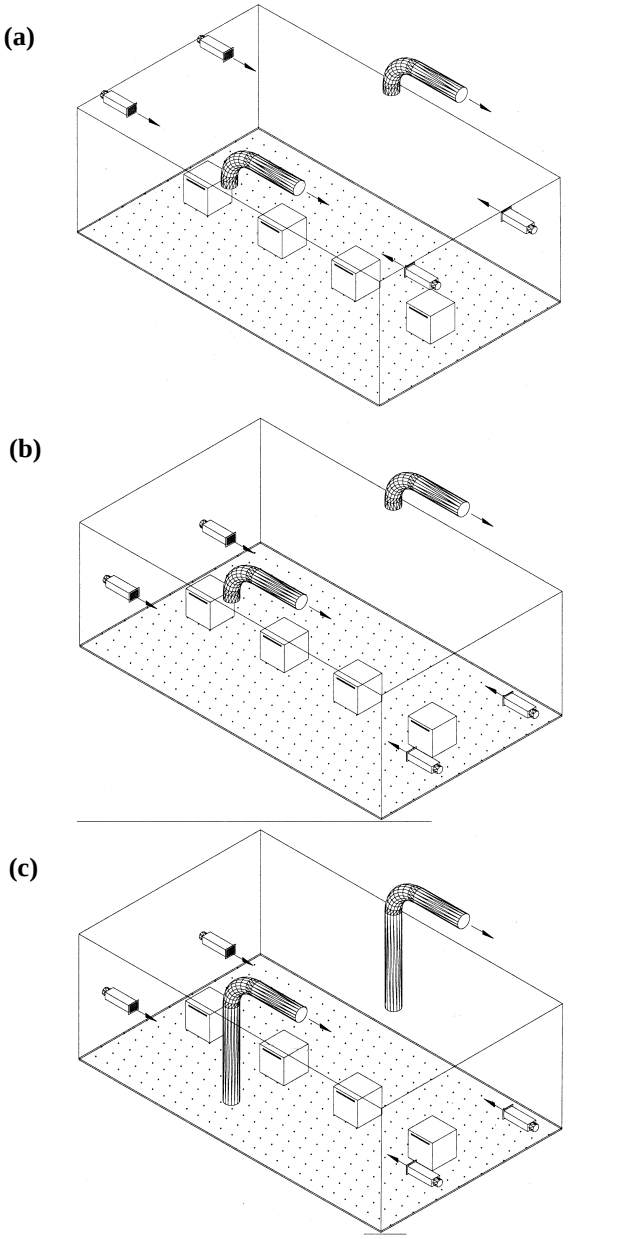

Figure 2 *Opposite wall configuration. (a) Opposite wall grille, high-high; (b) opposite wall grille, low-high; (c) opposite wall grille, low-low.*

heights for the small-scale experiment are tabulated in Table 2, along with the corresponding full-scale values.

The industrial processes were modeled with 2 ft cubes constructed from sheet metal, as shown in Figure 4. The cube size corresponds to 8 ft × 8 ft × 8 ft (2.4 m × 2.4 m × 2.4 m) full-scale processes. The processes were modeled not as specific industrial processes but as generic processes through which room air was circulated and which released heat and contaminants. The heat source in the cube was an internal electric heater with a constant velocity fan. The heaters had a maximum power output of 1500 W. The power output was controlled by variable voltage supplies and was checked by simultaneous voltage and current measurements.

As shown in Figure 4, each cube had an open slot 1.5 in. high by 1 ft wide located on the bottom of the back side of the cube to serve as an air inlet. Each cube also had an open slot, of the same dimensions, on either side and 2 in. from the top to serve as air and contamination outlets. The contamination source was CO_2 gas. The CO_2 was introduced into the heated flow using a perforated ping pong ball so that it was well mixed with the heated flow inside the cube.

Depending on which ventilation configuration was used, one of two industrial process configurations was used: line or

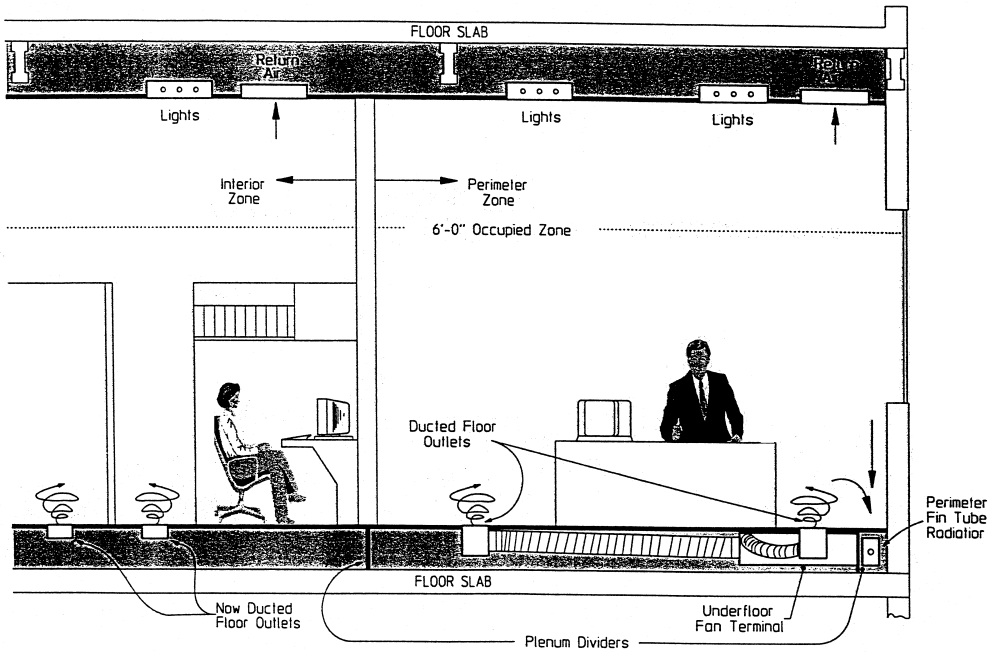

Figure 1 *Typical underfloor air distribution system.*

Overhead mixing type systems (see Figure 2) have been very popular for the conditioning of office space in North America. These systems supply conditioned air to the space by means of ceiling-mounted diffusers. These diffusers discharge air along the ceiling at 55°F to 57°F (13°C to 14°C) and are sized for sufficient outlet velocities to induce room air, mixing this with the supply air prior to entry into the occupied regions of the space. Most of the heat transfer between supply and room air occurs above the 6 ft (1.8 m) level. When properly selected, these outlets produce resultant room velocities in the 20 fpm to 30 fpm (0.10 m/s to 0.15 m/s) range throughout the occupied zone (the lower 6 ft or 1.8 m of the space). Proper outlet selection results in (1) little or no temperature gradient within the occupied zone, (2) return air temperatures (at the ceiling) that are similar to that of the room itself, and (3) similar contamination levels throughout the space (and in the return airstream) at design conditions.

Underfloor air distribution systems (also illustrated in Figure 2) typically supply air at discharge temperatures between 58°F and 63°F (14°C to 17°C) utilizing special high induction floor diffusers. This is particularly important as supply air is being introduced within the occupied regions of the space, so it is necessary that discharge velocities and temperatures be significantly reduced before occupants within

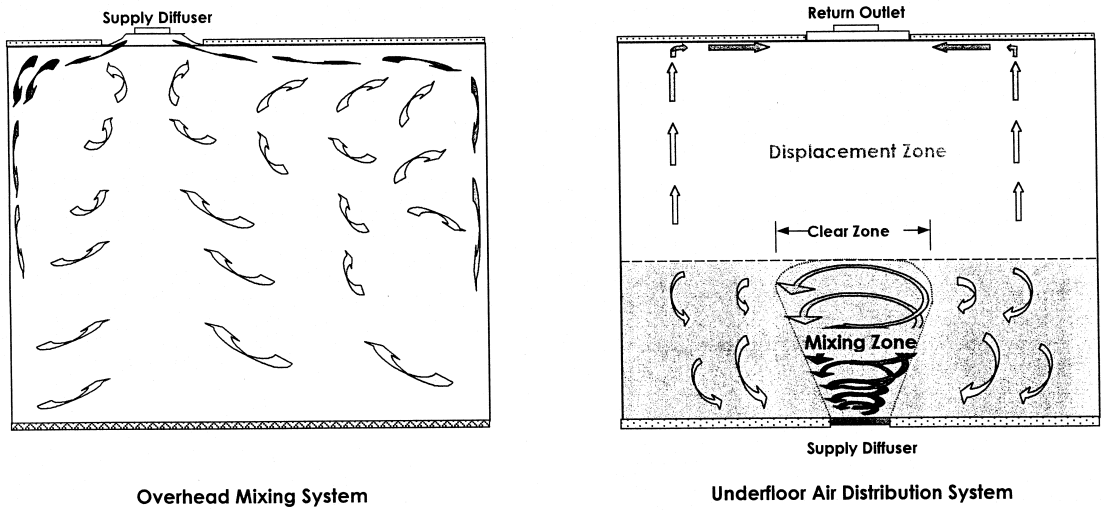

Figure 2 *Overhead and underfloor air distribution systems.*

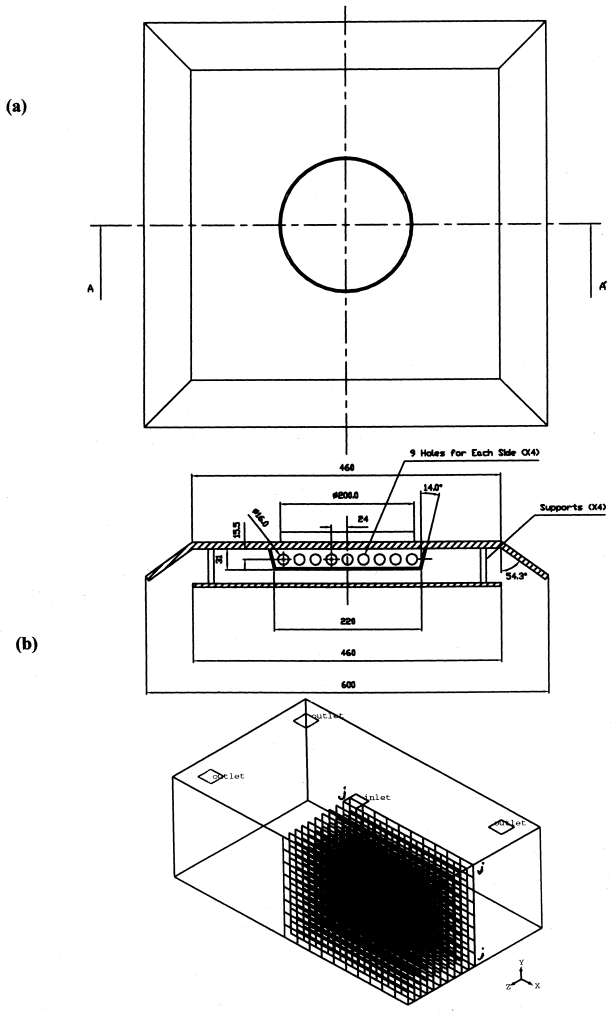

Figure 1 *(a) A four-way nozzle type diffuser; (b) volume studied. Unit: mm.*

ceiling nozzle type diffuser (cases 1 through 3). In this study, the wall-mounted nozzle type diffuser with an inclined angle of 15°, located at the level of 1.0 m from the floor, has two openings with effective areas of 1.29×10^{-3} and 0.32×10^{-3} m^2, respectively. The wall-mounted diffuser is assumed to handle a quarter volume of the environmental chamber. For case 7 and case 8, only the larger opening is used. For case 9, with a high supply flow rate, both openings are used. In order to understand the influence of supply air temperature on airflow performance and thermal comfort for the ceiling nozzle type diffuser, three cases (case 10, case 11, and case 12) have been tested with 4°C cold air. The sensible heat load and latent heat load is the same as that of case 1, case 2, and case 3.

Part 3—Simulation for a Multi-Cone Circular Diffuser (Case 13 through Case 17)

Detailed studies of a multi-cone circular diffuser are lacking in the literature. Recently, Hirano et al. (1997) conducted a very detailed measurement of the airflow and turbulence characteristics in the outlet vicinity of a multi-cone circular diffuser using two sets of crossed hot wire anemometers. A fairly symmetrical airflow pattern was observed. Therefore, Hirano's experimental data are used to validate the present airflow model. The geometry of the multi-cone circular diffuser (with two cones) experimentally studied by Hirano et al. is shown in Figure 2a.

Table 2 summarizes the simulation cases for a multi-cone circular diffuser (with three cones, as shown in Figure 2b). Cases 13 through 15 aim to compare air diffusion characteristics of jets created by the multi-cone circular diffuser under various supply flow rates. The objective of case 16 was to determine the effect of the small hole on the risk of surface condensation on the diffuser. The purpose of case 17 was to assess the effect of the cone lip on the performance of air diffusion using a multi-cone diffuser.

NUMERICAL METHOD AND BOUNDARY CONDITIONS

For cases 1 through 12, because of the symmetry of the airflow patters in the environmental chamber, only a quarter volume of the room was studied, as shown in Figure 1b. It is

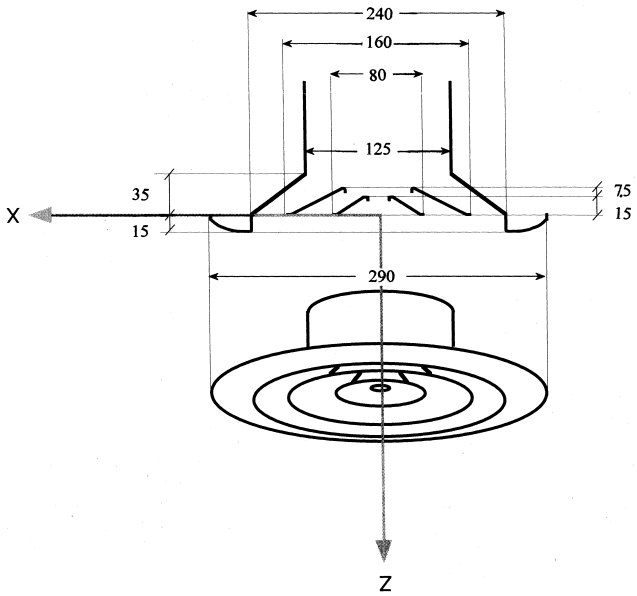

Figure 2a *The multi-cone circular diffuser measured by Hirano et al. Unit: mm.*

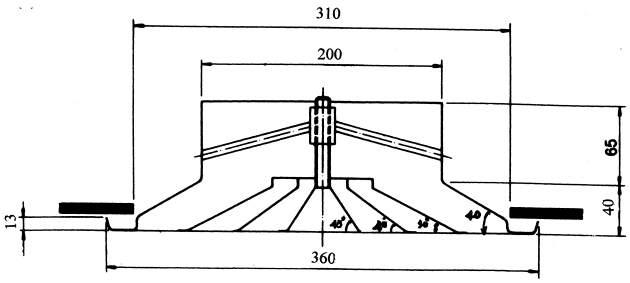

Figure 2b *The multi-cone circular diffuser studied in cases 13 through case 1. Unit: mm.*

TABLE 3
Criteria for Equivalent Stack Height (ESH) Selection

Location of Maximum Concentration	Description
1	If the screen test maximum concentration is located inside the screen, criterion A must be met by any one ESH concentration inside the screen (not necessarily at the same string distance as the screen test maximum concentration). Criterion B must be met by all ESH concentrations outside the screen.
2	If the screen test maximum concentration is located outside the screen, criterion A must be met by any ESH concentration outside the screen (not necessarily at the same string distance as the screen test maximum concentration). Criterion B must be met by all ESH concentrations outside the screen. Criterion C must be met by any ESH concentration inside the screen (not necessarily at the same string distance as the maximum screen test concentration).
Criteria	
A	The maximum concentration of the ESH must meet or exceed the maximum concentration of the screen test.
B	The ESH concentration must be greater than or equal to 80% of the screen test concentration.
C	The ESH concentration inside the screen must be greater than or equal to 80% of the maximum screen test concentration inside the screen.

$$\text{SHR} = (0.0081 \times \text{Porosity}) + 0.20 \qquad (6)$$

where porosity is in percent. Use of the above equation produces the calculated SHR factors in Table 4.

Now, with a general equation for estimating the SHR factor, the effect of an architectural screen on rooftop dilution can be estimated. First, the stack and screen design parameters are specified. Second, the SHR is calculated using Equation 6. Next, the height to spread parameter is modified as follows,

$$Y = 28.9\left(\frac{(SHR)h_s}{S}\right)^2, \qquad (7)$$

and is used in the Handbook (ASHRAE 1997) calculations.

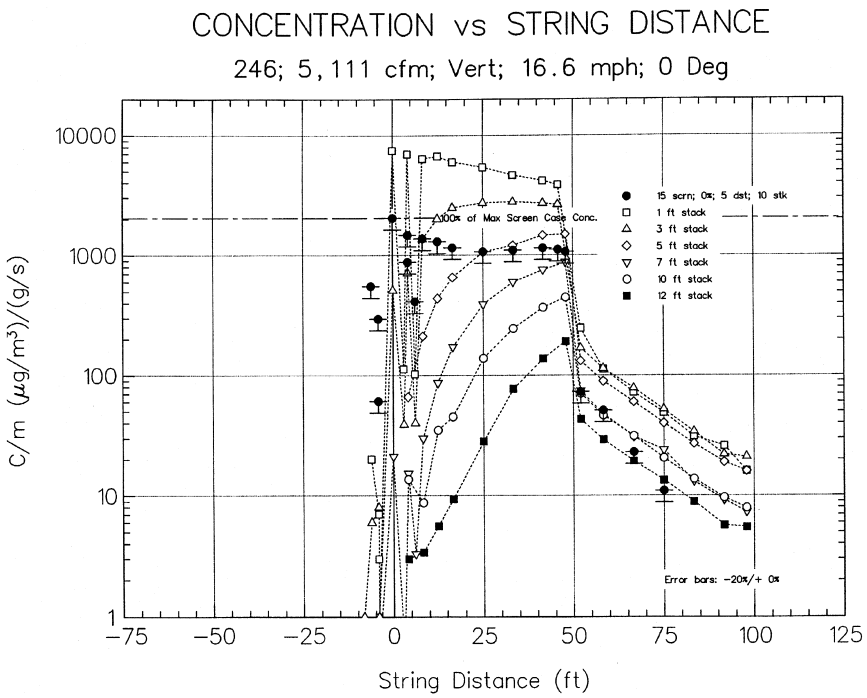

Figure 3 *Full-scale concentration vs. string distance (µg/m³ per g/s); run 246; 15 ft screen height; 0% screen porosity; 5 ft screen distance; 10 ft stack height; 5,111 cfm; vertical stack orientation; 16.6 mph wind speed; 0° wind direction.*

TABLE 4
Test Summary for Fire Sizes Larger than 3 MW (2800 Btu/s) for the 22 m (73 ft) Facility*

Test Number	Pan Size m (ft)	Fire Size (1 ± 10%) MW (Btu/s)	Fuel Type	Sprinkler Act.† s (Wet Pipe) (QR 79°C)(175°F)	Smoke Det.Act.†s (P.B.‡/S.P.**) ± 10 s
14	2.5 (8.2) Dia	7.9 (7500)	JP-5	361.±10.	38/65.
15	3.0 × 3.0 (10 × 10)	15.7 (14900)	JP-5	119.±10.	33/46.
16‡‡	2.5 (8.2) Dia	7.0 (6600)	JP-5	No	T††/51.
17	3.0 × 3.0 (10 × 10)	14.3 (13600	JP-8	100.±10.	27/30.
18	2.0 (6.6) Dia	4.9 (4600)	JP-5	No	42/49.
19‡‡	2.5 (8.2) Dia	9.1 (8600)	JP-5	No	39/56.
20	3.0 × 3.0 (10 × 10)	14.6 (13800)	JP-5	101.±10.	31/38.
21	4.6 × 4.6 (15 × 15)	33 (31000)	JP-5	87.±10.	30/37.

* The sprinklers were located 3.1 m (10 ft) from plume center.
† Activation times represent the first time that a detector activated at that distance from the fire. Activation times for detectors should include a ±10 s uncertainty in establishing the start time of the experiment.
‡ Denotes a projected beam detector with the beam located 1.3 m (4.3 ft) below the ceiling and passing through plume center.
** Denotes a single-point smoke detector located 3.1 m (10 ft) from plume center.
†† Trouble signal.
‡‡ Open door test.

The primary roof support consisted of a series of steel trusses that form arches spanning the width of the hangar bay, running parallel to the hangar doors. These primary trusses are approximately 1.0 m (3.3 ft) deep and are spaced 7.4 m (23 ft) on center. The primary trusses are interconnected with a series of secondary trusses that are perpendicular to them and run the length of the hangar bay. The secondary trusses are spaced at intervals ranging from 5.8 m (19 ft) to 6.4 m (21 ft) on center. The metal deck roof is directly attached to a series of steel beams that sit on top of the primary and secondary trusses. These steel beams are perpendicular to the primary trusses, are spaced 1.5 m (5 ft) to 2.1 m (7 ft) on center, and vary in height from 0.2 m (8 in) to 0.3 m (12 in).

The roof was insulated via a barrel-shaped suspended tile ceiling that was supported by a conventional suspended tile ceiling grid located at the same elevation as the bottom of the steel beams. The ceiling tiles were removed in the middle bay and the adjacent bays prior to testing.

Experimental east and west were designated to be the directions parallel to the 13.4 m (44.0 ft) draft curtain and pointed along the direction of the barrel roof. Experimental north and south directions ran perpendicular to the draft curtain. Thermocouples located 0.31 m (1.0 ft) beneath the ceiling were at radial distances from the fire center of 3.0 m (10 ft), 4.6 m (15 ft), 6.1 m (20 ft), and 6.7 m (22 ft) in the south direction and 3.0 m (10 ft) and 6.1 m (20 ft) in the north direction. Thermocouples located 0.31 m (1.0 ft) beneath the ceiling were at radial distances from the fire center of 3.0 m (10 ft), 6.1 m (20 ft), 9.1 m (30 ft), 12.2 m (40 ft), 15.2 m (50 ft), and 18.3 m (60 ft). Additional thermocouples were positioned at many of these locations and are represented in Figure 3.

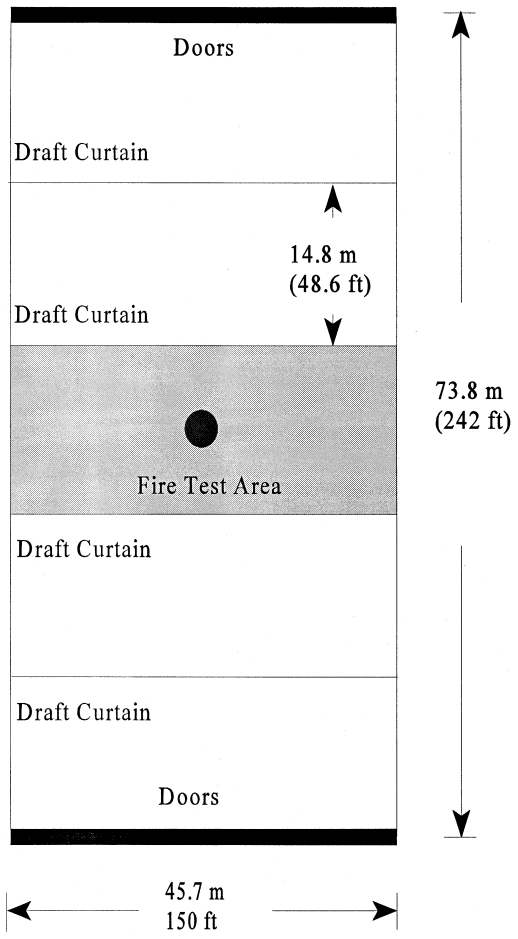

Figure 2 *Plan view of 22 m (73 ft) hangar.*

TABLE 4
Values Used for Tenability Discussions

Material	Flaming $LC\tau_{50}$ (g m^{-3} min)	Post-Flashover $LC\tau_{50}$ (g m^{-3} min)	Particulate Yield y_p	Chemical Heat of Combustion ΔH_{ch} (kJ/kg)
Wood (hemlock)	3120	750	0.015	13,300
PMMA	1200	530	0.022	24,200
PVC	300	200	0.098	7,700
Wool	920	70	0.008	19,500
Nylon	920	70	0.075	27,100
PU Foam (flexible)	1390	200	0.188	17,600
PU Foam (rigid)	100	54	0.118	16,900

$$T_s = \frac{T_a}{1 - \dfrac{\Delta H_{ch} K R}{C_p K_m y_p P}} . \qquad (21)$$

Equations 20 and 21 are independent of the heat release rate and the duration of the fire. These equations for FED and T_s are expressed as functions of K. Table 4 lists some materials for which the lethal exposure dose is available from Table 1 and the particulate yield is available from Table 3.

If the smoke from these materials is diluted so that K is 0.35 m^{-1}, visibility meets the criterion for this paper. For this visibility, the FED for flaming fires and post-flashover fires is shown in Figures 2 and 3. Flaming fires have unrestricted access to air, as can be expected of a fire in an open atrium, provided that the smoke layer is above the flames. While there are many definitions of the post-flashover fire, it can generally be said that the entire fire room is involved in fire.

In North America, most atria smoke management designs are based on protecting against a fire located in the atrium. This is based on the idea that fires in rooms or other spaces that are open to the atrium are protected by sprinklers. For these designs, the FED data for fires with unrestricted access to air (Figure 2) are appropriate.

Generally, atria are expected to be evacuated in less than 20 minutes with even less exposure time inside the atrium. From Figure 2, it can be seen that the FED values are less than 0.2 for all the materials evaluated with an exposure time of 30 minutes. As already stated, Figure 2 has sufficient dilution to provide acceptable visibility and a FED value of 0.5 indicates incapacitation. Thus, for any of these materials burning in an atrium, if the smoke is sufficiently diluted to meet the visibility criteria of this paper, toxicity is not a concern for exposure times less than 30 minutes. Figure 2 can be examined to see that for all these materials, the above statement includes a significant factor of safety.

In some locations (such as the United Kingdom) designs are based on protecting against fires in rooms or shops that open onto the atrium. For these designs, a post-flashover fire might occur and the FED data of Figure 3 could be appropriate. Post-flashover fires produce higher levels of CO, so it was expected that the FED values for post-flashover fires would be higher than those of fire with unrestricted access to air (Figures 2 and 3). With the exception of wool, it can be seen

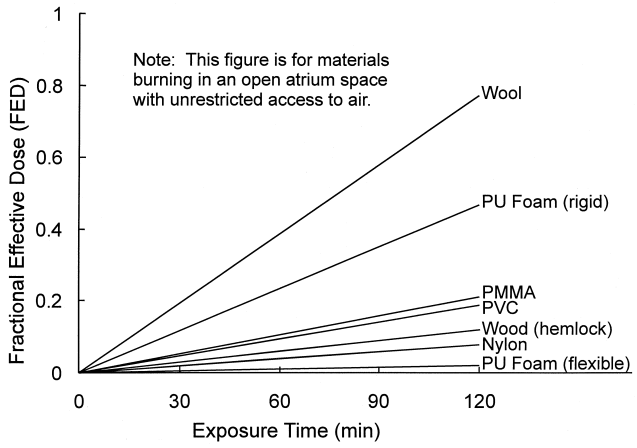

Figure 2 *FED produced by smoke of* K = *0.35 m^{-1} from fires in an atrium.*

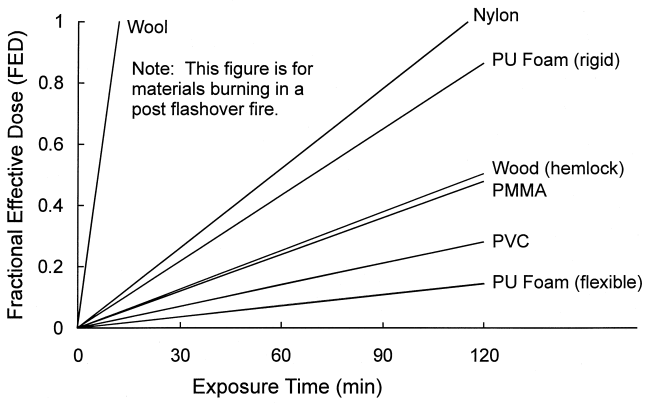

Figure 3 *FED produced by smoke of* K = *0.35 m^{-1} from post-flashover fires.*

buildings chosen also meet the site selection criteria, including two sites from each of three size ranges: small—less than 45 apartments; medium—45 to 80 apartments; large—greater than 80 apartments.

The project research buildings are characteristic of the older and predominant stock of the over 120,000 New York City multi-family buildings. Table 1 lists the sites and their size (in number of apartments).

TABLE 1
Project Buildings

ID#	Address	Apartments
12	Beach St.	25
31	Tinton Ave.	42
7	Burr Ave.	60
9	Buhre Ave.	80
10	Trinity Ave.	102
30	St. Theresa Ave.	103

The buildings ranged in size from 25 to 103 apartments in either five or six above-ground stories. All but one have combination steam and DHW-generating steel tube boilers. One site has a combination system with a cast iron boiler. DHW is generated by a "tankless coil" located under the surface of the boiler water.

All six buildings in this study had a forced recirculation system with the pump running continuously. Figures 1 and 2 depict representative DHW consumption and recirculation flow patterns found in the buildings.

Control Strategies

Data from a prior DHW modeling project (Goldner and Price 1996) suggested that it may not be necessary to continuously operate forced DHW recirculation systems in multi-family buildings, as is the practice in most buildings. The recirculation control research project detailed here measured the energy savings that can be realized by cycling these pumps using a base case of continuous operation and three other operating strategies:

a. *Base case (continuous operation)*: Strategy A is used as a base case against which to determine the savings achievable by the other approaches.

b. *Shutdown during the overnight period*: Strategy B's approach is to attempt to save energy by shutting down the pumps at night when few, if any, people are using hot water. After careful review of the data, it was determined that the pumps should be shut off from 11:50 p.m. to 5:20 a.m. each night.

c. *Shutdown during the peak morning and evening periods*: Strategy C's approach is to attempt to save energy by shutting down the pumps during the peak DHW usage periods, when the large volume of usage is, in and of itself, causing circulation to occur. Data review determined that the pumps should be shut off from 5:45 a.m. to 8:15 a.m. each morning and 5:45 p.m. to 9:15 p.m. each evening.

d. *Cycling by a return line aquastat*: Strategy D evaluates running the pump only when the DHW temperature in the basement return line falls below 110°F (61.1°C), as controlled by a return line aquastat.

PROJECT METHODOLOGY

Realizing that different buildings use varying volumes of DHW, it was essential that this research compare the effects of operating the DHW recirculation systems with each strategy at each of the six selected sites. These buildings were selected and equipped with the necessary pump control devices (both a return line mounted aquastat and a programmable timeclock, each wired into the recirculation pump) and monitoring equipment. This research project was designed to isolate those

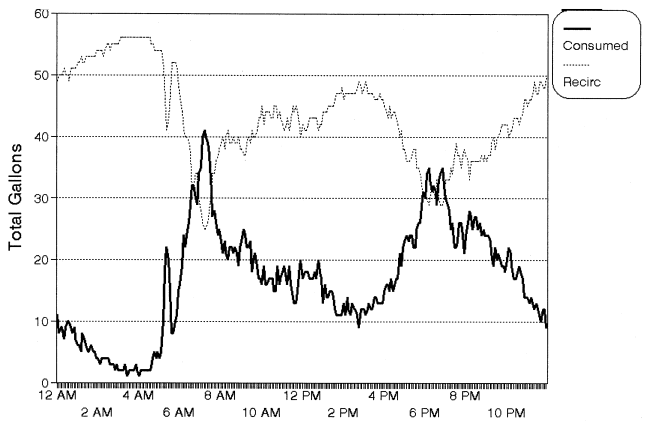

Figure 1 *DHW consumption and recirculation flows for Building 7, weekday.*

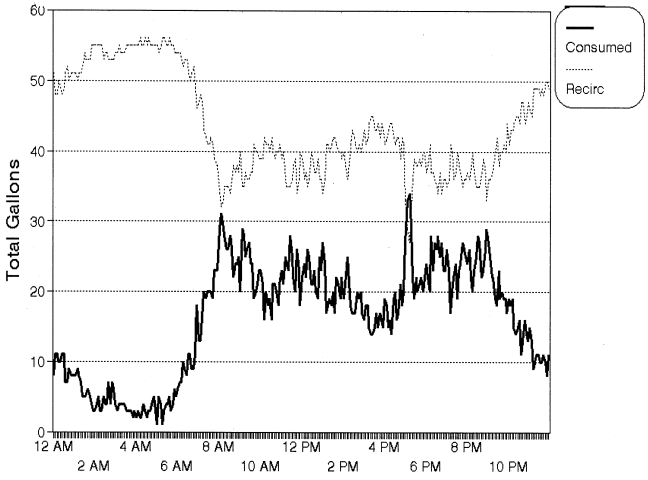

Figure 2 *DHW consumption and recirculation flows for Building 7, weekend.*

Table 1 Data for Determining Operating Characteristics of Snow-Melting Systems

City	Period of No Snowfall: % of Hours with No Snowfall[a] Air Temp. > 32°F	Air Temp. ≤ 32°F	Mean Air Temp. During Freezing Period,[d] °F	Wind Speed During Freezing Period,[d] mph	Period of Snowfall[b]: Hours of Snowfall[a,b] %	per Year	Free Area Ratio, A_r	Required Output,[c,g] Btu/h · ft²: 0 to 49	50 to 99	100 to 149	150 to 199	200 to 249	250 to 299	300 to 349	350 to 399	400 up	Maximum Output,[c,g] Btu/h · ft²
								Frequency Distribution of Snowfall Hours at Above Outputs, %[e]									
Albuquerque, NM	74.7	24.7	26.2	8.5	0.6	22	1	62.0	25.4	7.6	4.2	—	0.8	—	—	—	259
							0	94.1	5.9	—	—	—	—	—	—	—	82
Amarillo, TX	73.1	26.0	24.6	13.3	0.9	33	1	33.7	35.4	15.4	10.7	3.0	1.8	—	—	—	260
							0	88.1	19.1	1.8	—	—	—	—	—	—	143
Boston, MA	64.6	31.4	24.7	14.2	4.0	145	1	51.5	30.0	12.3	4.3	1.2	0.6	0.1	—	—	320
							0	83.2	14.0	2.0	0.3	0.3	0.1	—	0.2	—	370[f]
Buffalo-Niagara Falls, NY	46.5	46.9	23.9	10.8	6.6	240	1	50.7	32.6	11.2	3.7	1.4	0.2	0.2	—	—	309
							0	95.9	3.4	0.2	0.5	—	—	—	—	—	192
Burlington, VT	39.0	54.5	19.6	10.8	6.5	236	1	53.7	29.9	13.2	2.5	0.6	0.1	—	—	—	280
							0	91.8	7.6	0.6	—	—	—	—	—	—	142
Caribou-Limestone, ME	21.4	70.6	16.5	10.0	8.0	290	1	35.0	39.7	16.0	5.7	2.0	1.0	0.5	0.1	—	378
							0	92.0	7.5	0.5	—	—	—	—	—	—	138
Cheyenne, WY	46.4	49.8	21.5	15.3	3.8	138	1	16.5	26.2	19.4	13.1	8.6	4.7	4.2	4.7	2.6	499
							0	94.3	5.4	0.3	—	—	—	—	—	—	129
Chicago, IL	45.4	50.9	21.4	11.5	3.7	134	1	45.8	37.4	11.4	3.1	1.4	0.6	0.2	0.1	—	368
							0	91.5	8.1	0.3	0.1	—	—	—	—	—	165
Colorado Springs, CO	54.3	43.6	22.1	11.5	2.1	76	1	26.8	36.3	19.0	7.5	4.4	5.5	0.5	—	—	311
							0	98.4	1.6	—	—	—	—	—	—	—	63
Columbus, OH	59.0	38.1	24.5	10.0	2.9	105	1	65.8	22.4	8.0	1.7	1.7	0.4	—	—	—	261
							0	97.7	2.3	—	—	—	—	—	—	—	72
Detroit, MI	47.0	49.3	24.1	10.6	3.7	134	1	60.4	27.7	9.3	1.5	0.8	0.3	—	—	—	278
							0	95.9	3.5	0.6	—	—	—	—	—	—	140
Duluth, MN	12.6	80.5	14.5	12.0	6.9	250	1	23.7	32.9	20.6	13.7	4.3	2.5	1.7	0.6	—	382
							0	94.8	4.7	—	0.3	0.2	—	—	—	—	206
Flamouth, MA	68.5	29.5	25.5	12.8	2.0	73	1	50.0	33.9	14.2	1.6	0.3	—	—	—	—	204
							0	91.5	7.4	1.1	—	—	—	—	—	—	144
Great Falls, MT	49.0	46.2	16.5	14.4	4.8	174	1	26.2	27.6	16.7	16.4	7.5	4.6	0.3	0.5	0.2	451
							0	94.6	4.8	0.6	—	—	—	—	—	—	138
Hartford, CT	56.4	38.9	24.4	8.2	4.7	171	1	48.4	34.6	11.2	4.3	0.8	0.7	—	0.1	—	396
							0	80.4	16.7	2.2	0.5	—	0.1	—	0.1	—	383
Lincoln, NB	45.0	52.5	20.8	10.1	2.5	91	1	32.7	26.2	20.0	13.9	5.7	1.5	—	—	—	293
							0	97.2	2.6	—	—	0.2	—	—	—	—	202
Memphis, TN	87.2	12.5	27.0	11.5	0.3	11	1	48.4	28.3	6.7	13.3	3.3	—	—	—	—	227
							0	85.0	8.3	6.7	—	—	—	—	—	—	144
Minneapolis-St. Paul, MN	23.6	70.8	16.9	11.1	5.6	203	1	28.4	31.4	21.7	14.1	3.5	0.6	0.3	—	—	313
							0	96.5	3.1	0.3	0.1	—	—	—	—	—	155
Mt. Home, ID	56.3	42.6	24.9	9.5	1.1	40	1	74.2	21.9	3.9	—	—	—	—	—	—	143
							0	98.1	1.9	—	—	—	—	—	—	—	90
New York, NY	55.7	42.2	24.2	11.8	2.1	76	1	53.1	31.8	9.4	2.2	1.5	1.7	—	0.3	—	385
							0	87.6	9.6	1.5	0.7	0.3	0.3	—	—	—	298
Ogden, UT	50.0	45.6	24.3	9.4	4.4	160	1	64.6	29.2	5.8	0.3	0.1	—	—	—	—	216
							0	88.8	9.4	1.4	0.3	0.1	—	—	—	—	216[f]
Oklahoma City, OK	79.0	19.8	24.6	15.8	1.2	44	1	27.8	18.7	17.0	12.6	14.3	5.9	2.7	1.0	—	394
							0	95.7	4.3	—	—	—	—	—	—	—	81
Philadelphia, PA	75.8	22.6	26.7	9.7	1.6	58	1	62.3	23.6	10.4	2.3	0.9	0.5	—	—	—	296
							0	84.3	14.0	1.1	0.2	0.4	—	—	—	—	229
Pittsburgh, PA	55.2	39.8	24.3	11.6	5.0	182	1	53.6	30.8	8.4	4.6	1.9	0.7	—	—	—	282
							0	93.3	5.9	0.7	0.1	—	—	—	—	—	157
Portland, OR	92.9	6.1	28.9	8.4	1.0	36	1	78.0	16.9	5.1	—	—	—	—	—	—	125
							0	91.5	8.5	—	—	—	—	—	—	—	97
Rapid City, SD	45.2	51.6	19.3	12.9	3.2	116	1	29.7	29.0	16.0	8.4	6.3	3.6	1.9	2.0	3.1	581
							0	97.6	2.2	0.2	—	—	—	—	—	—	102
Reno, NV	56.0	41.6	24.3	5.6	2.4	87	1	82.6	15.4	1.8	0.2	—	—	—	—	—	152
							0	90.2	8.0	1.6	0.2	—	—	—	—	—	154[f]
St. Louis, MO	68.7	30.4	25.0	11.5	0.9	33	1	42.9	31.4	16.7	7.1	1.9	—	—	—	—	225
							0	85.2	11.6	2.6	0.6	—	—	—	—	—	152
Salina, KS	60.0	38.5	23.3	10.9	1.5	54	1	44.9	31.9	12.7	7.6	2.2	0.7	—	—	—	286
							0	93.5	6.2	0.3	—	—	—	—	—	—	120
Sault Ste. Marie, MI	21.3	69.2	18.6	9.4	9.5	345	1	45.7	32.8	14.3	5.7	1.4	0.1	—	—	—	262
							0	97.9	2.0	0.1	—	—	—	—	—	—	144
Seattle-Tacoma, WA	88.0	10.8	28.5	5.9	1.2	44	1	86.3	12.3	1.4	—	—	—	—	—	—	137
							0	91.0	8.1	0.9	—	—	—	—	—	—	128
Spokane, WA	48.5	46.1	25.7	10.7	5.4	196	1	62.6	28.7	7.4	1.1	2.0	—	—	—	—	205
							0	92.0	7.8	0.2	—	—	—	—	—	—	127
Washington, D.C.	77.9	21.2	26.8	9.6	0.9	33	1	59.0	29.8	10.6	0.6	—	—	—	—	—	154
							0	85.7	11.8	2.5	—	—	—	—	—	—	121

Source: Air Conditioning, Heating and Ventilating, August, 1957, p. 87.

Note: The period covered by this table is from November 1 to March 31, with February taken as a 28.25-day month. Total hours in period = 3630.

[a]The percentages in Columns 2, 3, and 6 total 100%. Note that Hours of Snowfall per Year does not include idling time and is not actual operating time. See text.

[b]Snowfalls of trace amounts are not included; hence, only those hours of 0.01 in. or more water equivalent snowfall per hour are listed.

[c]Output does not include allowance for back or edge losses because these depend on slab construction.

[d]Freezing Period is that during No Snowfall when the air temperature is 32°F or below.

[e]Percentages total 100% of the number of hours of snowfall.

[f]When heat output for $A_r = 0$ equals or exceeds the heat output for $A_r = 1$, the heat transfer q_h is from the air *to* the slab. This occurs when snowfall is at temperatures above 32°F.

[g]Multiply output values by 0.293 to convert to W/ft².

Figure 2 *Table 1 as it appears in the* 1995 ASHRAE Handbook—HVAC Applications.

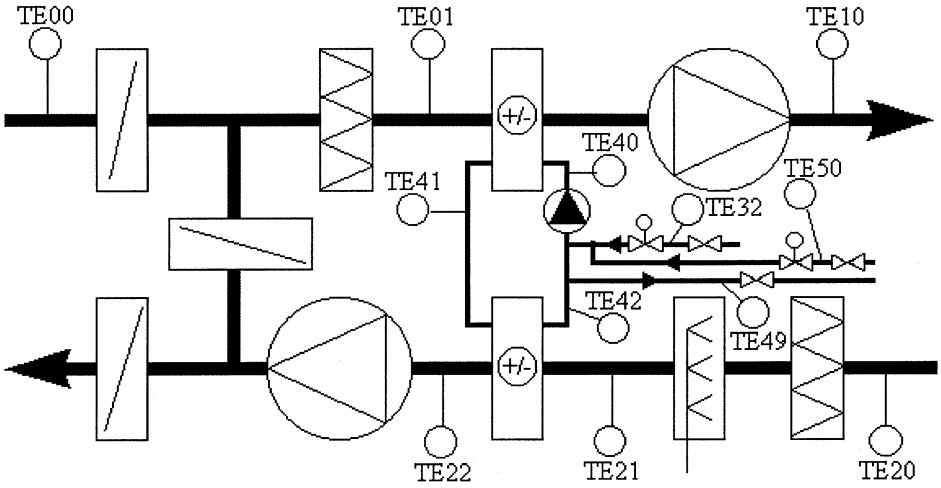

Figure 2 *A schematic diagram of one possible air-handling unit. The supply air side is drawn on upper side.*

device is tested separately, more reliable reference data are available for fault detection and diagnosis (FDD). The installation and commissioning phases should be performed based on specific plans made for these tasks. During operation and maintenance, the most essential parts of the system should be monitored and controlled. From each life-cycle phase, feedback is obtained that can be used in developing second-generation products and also during operation and maintenance of existing equipment.

This paper describes the process of how the performance factors for one brand of commercial AHU are established, how the performance requirements are defined based on these performance factors, and how these criteria can be connected to practical FDD methods in different life-cycle phases. In addition, this paper suggests several methods that can be used for performance monitoring. Examples of the implementation of the most promising methods are also given.

Figure 2 shows a schematic diagram of one possible AHU. The system considered includes fans and AHU components for

- air filtering,
- heating,
- heat recovery,
- indirect humidification (if required),
- cooling (if required), and
- air mixing.

The system is called a "building service unit" and it uses variable air volume. The heart of the building service unit is the liquid circulated heat recovery unit, which is used for both heating and cooling. Extra cooling capacity is available through indirect humidification (humidifier in the return airstream) and from the heat transfer network. Various heat sources are available. Often the heating capacity of the exhaust air and waste heat from refrigerators (condensing water) are the primary heat sources. District heating is also frequently used as a heat source.

LINKING PERFORMANCE FACTORS TO FAULT DETECTION AND DIAGNOSIS

Figure 3 illustrates how performance factors are connected to fault detection. The boxes in the figure represent the process from defining performance factors to the detection of faults. Under the boxes there are examples of possible contents of each box. For example, indoor climate, energy consumption, maintenance costs, and system reliability are performance factors for air-conditioning systems. When a particular system is considered, certain criteria for these factors can be given or specified, e.g., supply air temperature set points, outdoor air requirements, and air purity criteria. The criteria can be based on building codes, design requirements, and/or user requirements. Matsunawa et al. (1996) discussed the cost/benefit analysis of a building optimization

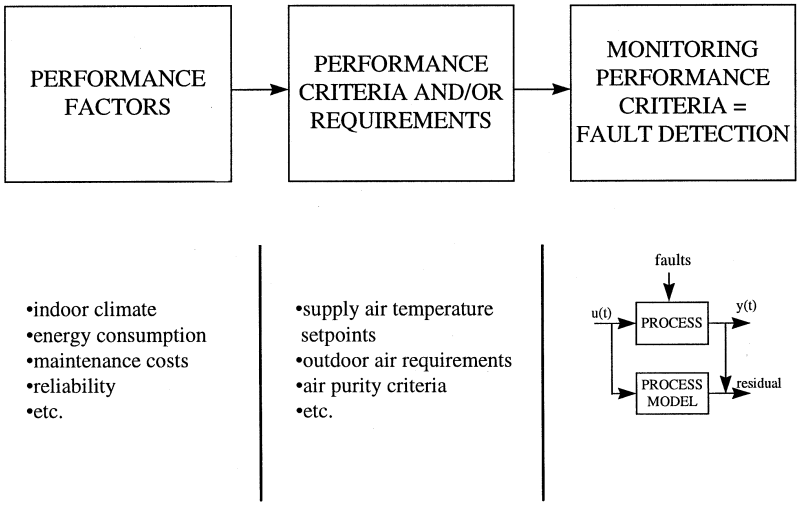

Figure 3 *Connection of performance factors to fault detection.*

TABLE 1
Energy Savings Estimated by Each of the Three Analysis Techniques

Technique	Control Comparison	DOE2 Model	Monitoring Results (Including Lot Lights)	Monitoring Results (Excluding Lot Lights)	Overall Estimate
Estimated Savings	18%	9%	18%	14%	12%-18%

The control wires for each of the ballasts used at the demonstration restaurant were terminated with a standard RJ11 telephone style connector that allowed for a simple plug-and-play interconnection of the ballasts with each other and with the photosensors (Figures 3 and 4). Other control devices, such as dimmers, could also be added to this system. In addition, this system used a single photosensor to control lighting fixtures on different electrical circuits, making zoning and rezoning a simple task.

These innovations dramatically reduced the initial cost for this system, bringing the installed cost in line with the standard, noncontrollable systems. At the demonstration restaurant, the system saved over 7,000 kWh/yr (25.2 GJ/yr) in the play area and dining areas (PG&E 1996-97), resulting in a payback of less than one year. Although ideal for new construction, controllable ballasts can also be considered during a retrofit of an existing restaurant. Figure 5 shows a typical dimming load profile in response to available daylight.

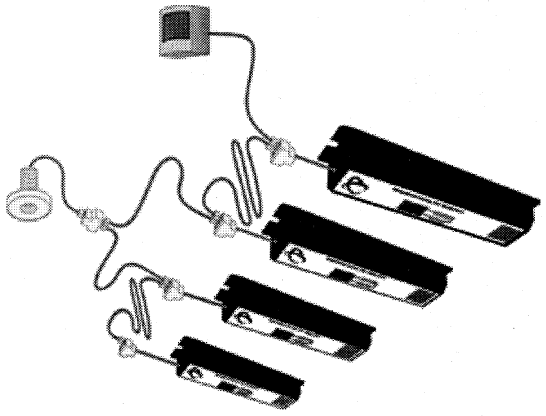

Figure 3 *Easily installed controllable ballast system.*

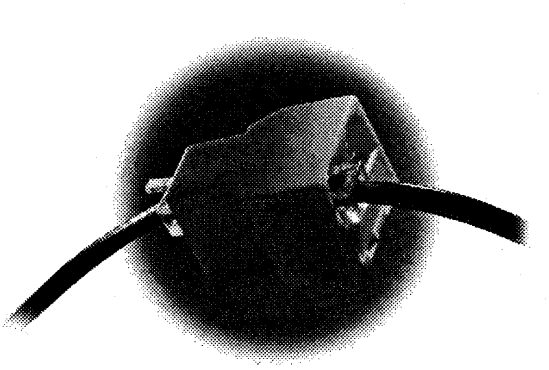

Figure 4 *Standard RJ11 connector used on ballast control wiring.*

LIGHT PIPES

Light pipes are tubular skylights that bring daylight into a restaurant. They are particularly effective in windowless spaces, such as restrooms, kitchens, and storerooms, but can also be used to brighten up darker areas of a dining room or improve the lighting quality at a service counter. Light pipes are unique because they can be used in applications where a full-sized skylight could not be used for reasons of available space or security. Also, the reflective pipes can be installed at an angle between the roof and the interior ceiling and the distance between the roof and ceiling can vary greatly without appreciable degradation of the light delivered at the diffuser dome.

Light pipes save energy when used in combination with electronic controllable ballasts by increasing the amount of available daylighting within the restaurant. The light pipes installed at the demonstration restaurant were 13 in. in diameter. Four of the six light pipes used in the demonstration restaurant were applied in areas that already had sufficient daylighting, so their contribution to energy savings was secondary to their aesthetic value. In a follow-up application at another restaurant, the experience gained at the demonstration restaurant was used to better locate the light pipes in several windowless spaces, including the kitchen, store rooms, and restrooms, where they had more effect on the electronic controllable ballasts. A sectional view of a light pipe is shown in Figure 6.

LOW-TEMPERATURE OCCUPANCY SENSORS

The lighting in walk-in coolers and freezers is typically left on all the time because of inconvenience and lack of incentive for manual switch control. There may be anywhere from one to six fixtures in a standard QSR walk-in, which are typically lamped with 75 W incandescent bulbs. Low-temperature occupancy sensors save energy by automatically turning the lights off in the walk-in cooler and freezer when they are unoccupied.

At the demonstration restaurant, the low-temperature occupancy sensors paid for themselves in less than a year, saving 3,265 kWh/yr (11.75 GJ/yr)—an 80% reduction in energy use (PG&E 1996-97). One sensor controlled the two fixtures in the walk-in cooler, and a second sensor controlled the four fixtures in the freezer. Additional savings were achieved by reducing the heat load on the refrigeration

Weather

Figure 2 shows the differences between the monthly average dry-bulb temperature for the Antioch weather file and the Bay Point weather file. In general, Bay Point was several degrees warmer during the winter and swing seasons compared to the Antioch WYEC2 weather. This may be due, in part, to the location of the Bay Point weather instrumentation, which was on the roof of the store. The store and its surrounding parking lot may serve as a heat "island" that causes elevation of the ambient temperatures. It may also be true that the conditions in Bay Point were usually warmer in the winter and swing seasons than in Antioch. From a modeling viewpoint, this is an area that deserves additional research.

Figure 3 shows the differences in monthly average humidity ratios for two weather files. Moisture conditions were reasonably similar during the year, except during late fall/early winter.

Lighting

The interior lighting systems in the baseline restaurant and the EEM restaurant used fluorescent T-8 lamps with electronic ballasts. The electric lighting system in the EEM design was enhanced with two energy efficiency measures:

- Daylight harvesting using dimming ballasts with daylight sensors in two zones in the dining room, the restrooms, and two zones in the play area.
- Six tubular skylight fixtures, also called "light pipes," two over the customer order counter, two in the play area, and one each in the two customer restrooms.

For daylight harvesting control, the dining zone was split into two parts, one toward the front windows and one toward the interior space close to the restrooms. The dining zone had two light sensors that permitted the electronic dimming ballasts in each zone to reduce power if sufficient daylight was available. The play area was also divided into two parts, each controlled by separate daylight sensors. Daylight harvesting in each restroom was dependent on the presence of a light pipe. Each restroom had a fiber-optic light sensor that permitted one fixture adjacent to the wash basins to operate at reduced power if sufficient light was available from the light pipe.

Daylight harvesting was modeled as an independent measure, but the light pipes were modeled assuming the daylight harvesting measure was in use. The light pipes consisted of vertical tubes that penetrated the roof and terminated below the ceiling tile with a translucent hemispherical diffuser. Sunlight, or available daylight on cloudy days, was transmitted through the light pipe, providing better quality light and reducing the amount of electric lighting needed in the immediate vicinity.

Table 5 shows the connected lighting power in each of the interior zones. The lighting circuits in the building were controlled by an energy management system through which the restaurant management could set on/off times by day of the week. The exterior accent lighting on the building totaled 1.9 kW. The parking lot lights totaled 15.0 kW in the initial model and were controlled by a photosensor, which turned them on when light levels fell below a predetermined level, and a timer, which turned them off after business hours. In the model, the exterior accent lighting and the parking lot lighting were scheduled according to weekday and weekend operating times, as well as seasonal changes in available sunlight (in the morning and the evening).

Model Calibration and Validation Changes for Lighting. Measured data showed that the aggregated, interior light-

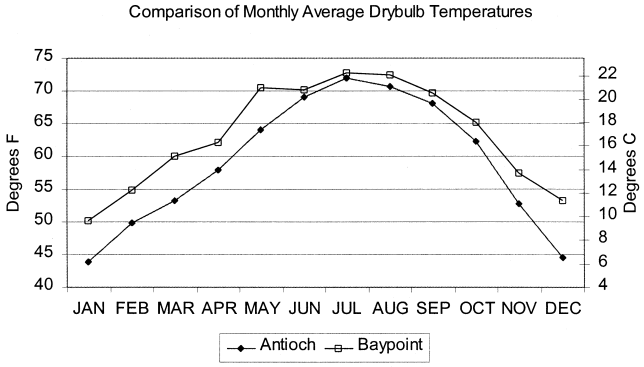

Figure 2 *Comparison of Antioch and Bay Point dry-bulb temperature.*

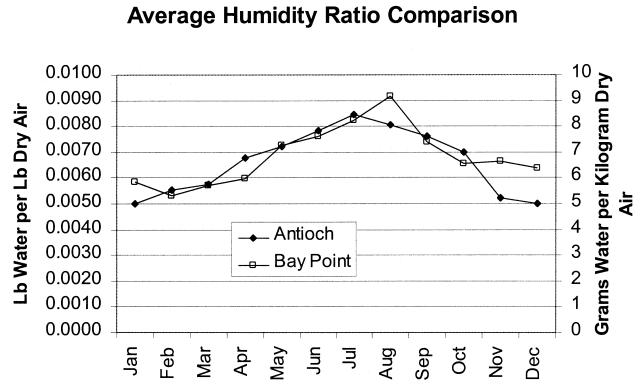

Figure 3 *Comparison of Antioch and Bay Point humidity ratio.*

TABLE 5
Lighting Power by Zone

Zone	Lighting Power (w/ft^2)	Lighting Power (w/m^2)
Kitchen	0.97	10.4
Dining (including restrooms)	1.28	13.8
Play area	1.08	11.6

TABLE 1
Backshelf Hood Exhaust Rates

Appliance→	"Clamshell" Griddle	
Vent Speed ↓ \ Op. Condition →	Idle/Standby	Cooking
1) Code flow rate:	1950 cfm (920 L/s)	1950 cfm (920 L/s)
2) Custom hood flow rate:	1255 cfm (592 L/s)	1255 cfm (592 L/s)
3) Custom hood two-speed:	630 cfm (297 L/s)	1255 cfm (592 L/s)

hood. For the demonstration restaurant with a two-speed system over the "clamshell" griddles, the high-speed exhaust rate was 1255 cfm (592 L/s) vs. the applicable code value of 1950 cfm (920 L/s). The two-speed exhaust fan also saves energy by turning down the exhaust when the clamshell griddle is in standby mode. Since this griddle is primarily used for batch cooking, there are significant amounts of time when it is in a standby or idle mode (Spata and Turgeon 1995). Under low-speed operation, the exhaust rate was 630 cfm (297 L/s). Table 1 compares the exhaust ventilation rate scenarios used for this QSR cost-saving comparison.

The energy consumption for scenarios 1 and 2 were calculated using the OALC for outdoor airflow rates that matched the exhaust rates shown in Table 1. For scenario 3, one initially would think that precise knowledge of the schedule would be necessary. Figure 4 plots the power input of the two-speed exhaust fan over a typical day. The 0.25 kW line represents operation at low speed, and the 0.45 kW data points represent operation at high speed. The data points in between are caused through time averaging, when the system was operating at high speed and low speed during part of the same measurement cycle. The plot shows rather random high and low periods throughout the day. Averaging the daily fan power profile for a month shows that the high/low profile turns into a rather stable line at 75% of maximum fan power input. Knowledge of power input and flow for high- and low-speed settings

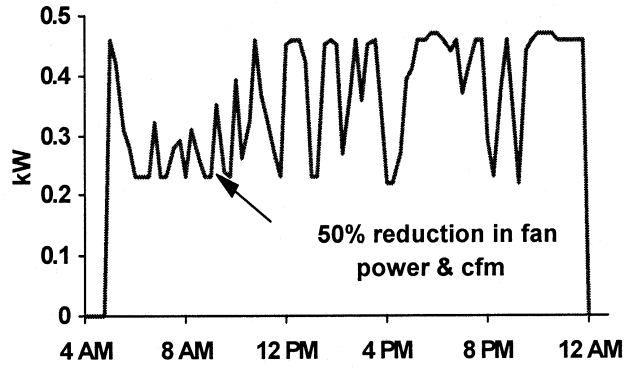

Figure 4 *Measured daily energy consumption profile for the two-speed exhaust fan.*

allows calculation of an effective flow rate at 75% of fan power as follows:

The effective power (= average power) is 75% of maximum input:

$$P_{eff} = 0.75 \cdot 0.45 \text{ kW} = 0.3375 \text{ kW}.$$

The average fan power is the fraction of time on low multiplied by the low power input plus the fraction of time with the fan on high times the power consumption on high.

$$P_{eff} = t_{low} \cdot 0.25 \text{ kW} + t_{high} * 0.45 \text{ kW}.$$

Since the total of time on low fraction and time on high fraction needs to be one ($t_{low} + t_{high} = 1$), the previous equation can be rewritten as

$$P_{eff} = t_{low} \cdot 0.25 \text{ kW} + (1 - t_{low}) \cdot 0.45 \text{ kW}.$$

The result of this equation is

$t_{low} = 56\%$,
$t_{high} = 44\%$.

So we can calculate an effective flow rate:

$$Flow_{eff} = 0.56 \cdot Flow_{low} + 0.44 \cdot Flow_{high}.$$

With the low flow rate being 630 cfm (297 L/s) and the high flow rate being 1255 cfm (592 L/s), the effective flow rate becomes 905 cfm (427 L/s). This effective flow rate allowed use of the OACL.

Energy Savings Estimates for the Optimized Two-Speed Exhaust System

This example is based on a demonstration quick service restaurant in Bay Point, California, and a second QSR in Chicago, Illinois.To reflect locations in the U.S. with a significant heating load, the OALC calculation example is presented for the Chicago site (Figure 5). The QSR kitchen had two 3-ft griddles and a four-bank fryer station. Since the demonstration restaurant only had two-speed ventilation for the griddle, this paper only presents the savings potential of the griddle exhaust system. The total ventilation savings potential for the QSR is, of course, higher than reported in this paper since the fryer-hood system was also operated below the code rate. It also would be feasible to design the fryer hood to operate under a two-speed scenario.

The Application of Three Different Evaporative Cooling Strategies to a Quick Service Restaurant

Stuart S. Waterbury, P.E. **Tor E. Allen** **Richard Young**

ABSTRACT

This paper describes the application of evaporative cooling strategies to the kitchen HVAC outdoor air intake, dining area HVAC condensers, and to the total cooling of a large, separate play area in a quick service restaurant (QSR). The paper includes a discussion of the types of evaporative coolers used, including media and once-through water flow, as well as the benefits and shortcomings of evaporative cooling in a quick service restaurant application. Measured data were used to determine the performance of the systems and to develop models used to predict cooling season performance. The performance of all evaporative cooling strategies reduced energy consumption, but they all required adjustments and modifications during the evaluation period. Proper commissioning after installation would have ensured peak performance sooner.

INTRODUCTION

A large quick service restaurant (QSR) operation formed an advisory panel of energy efficiency and environmental experts to assist in creating an energy-efficient QSR concept. The QSR management planned to incorporate the energy efficiency concepts in four restaurants in different climatic zones. In cooperation with the QSR design and construction team, a California utility provided design and construction support for an energy-efficient QSR in Bay Point, California (PG&E 1998). Three different evaporative cooling technologies were installed in this restaurant to evaluate their performance and cost-effectiveness. The results were used to assist quick service restaurant designers and management in determining if these technologies should be included as a standard specification item in new stores or as an option and to determine if the technology is a cost-effective application in a retrofit situation.

Design Considerations

Although many evaporative cooling systems recirculate the water passing through the evaporative media using a sump, in this application all the evaporative cooling systems used a one-pass system with no recirculation. Controlling the water flow to the media is more important in a one-pass system to minimize the amount of water going down the drain. The initial setup of the water flow controls is critical, as it affects the water consumption and thermal performance of the system. The advantages of a one-pass system are lower maintenance costs and the elimination of a standing water sump, which is a potential health risk if maintenance is neglected. A potential disadvantage is higher water and sewage cost.

Evaporative Cooling Technologies

Three different evaporative cooling technologies were installed, including a direct evaporative cooler serving the play area, a direct evaporative precooler on the outdoor air intake of the kitchen HVAC unit, and add-on evaporative precoolers on the dining HVAC unit condensers. Descriptions of these technologies follow.

Kitchen Outdoor Air Evaporative Precooler. The 10 ton HVAC unit specified to serve the kitchen was retrofitted with an evaporative precooler on the makeup air inlet. The purpose of the evaporative precooler was to reduce the temperature of the air entering the unit, thus reducing the amount of mechanical cooling required to maintain acceptable conditions in the kitchen. The evaporative precooler consists of evaporative cooler media that cools the incoming

Stuart S. Waterbury is a senior engineer at Architectural Energy Corporation, Boulder, Colo. **Tor E. Allen** is a research engineer at PG&E Pacific Energy Center, San Francisco, Calif. **Richard Young** is lead engineer at PG&E Food Service Technology Center, San Ramon, Calif.

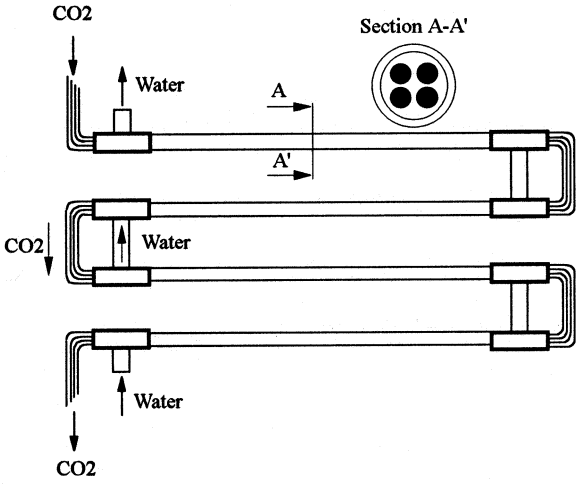

Figure 2 *Counterflow heat exchanger.*

A water-to-refrigerant counterflow heat exchanger was installed in this facility, as shown in Figure 2. In one shell, four refrigerant tubes were installed in parallel. The refrigerant mass flow rates within each tube are assumed to be the same. The heat exchangers were installed horizontally. The specifications for the evaporator and gas cooler are shown in Table 1.

Positive displacement compressor prototypes were designed and built, as shown in Figure 3. The design capacity of the prototypes was 11 kW. The original prototype, a hermetic compressor, was modified to have a removable lid to enable repairs and investigation of inner parts. More detailed design aspects can be found in Hwang and Radermacher (1998).

Instrumentation and Data Acquisition

Instrumentation and a data acquisition system were installed in the CO_2 test facility. CO_2 and water temperatures and pressures were measured at the locations indicated in Figure 1. Refrigerant mass flow rate, water volume flow rates, and compressor power input were also measured. Software routines to collect and analyze the data were developed. CO_2 refrigeration cycle performance was evaluated in terms of evaporator water-chilling capacity and coefficient of performance (COP). The water-side capacity and refrigerant-side capacity were evaluated and compared in each test to verify test results.

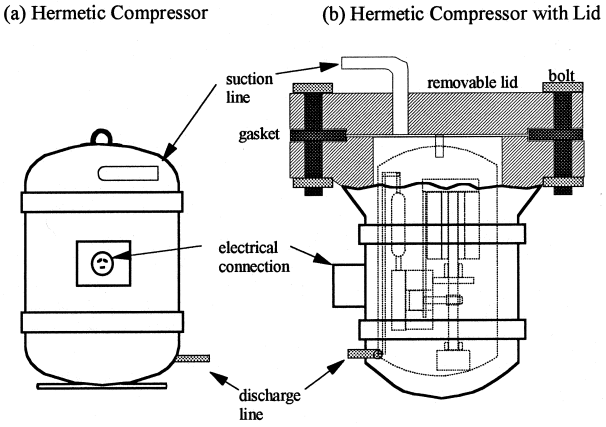

Figure 3 *CO_2 compressor prototype.*

Testing of Experimental Setup

Two steps were taken to verify the test facility's performance measurements. First, the water-side capacity measurement was verified with a 2 kW heater. The average error of the water-side capacity measurement relative to the heater power was less than 0.3%. Second, the refrigerant-side capacity and energy balance measurement were verified with conventional compressors. Two compressors for R-22 with 7 kW and 18 kW capacity were utilized for this purpose. The energy balance errors were within 4%, which is within the range of acceptable uncertainty for the experiment.

TEST RESULTS

Preliminary Charge Optimization with Prototype CO_2 Compressor

The prototype CO_2 compressor was tested with a counterflow heat exchanger. The results of the preliminary charge optimization tests are shown in Figure 4. In these tests, the metering valve opening was adjusted to vary the gas cooling pressure. The figure indicates that the 3.5 kg and 4.0 kg charges demonstrated higher performance than that shown by the 3.0 kg charge. The optimum charge was determined to be

TABLE 1
Specifications of Heat Exchangers

Heat Exchanger		Evaporator	Gas Cooler
Shell	Dimension (cm)	ID: 2.54 × t 0.165 × 600 (1 in. × 0.065 in. × 19.7 ft)	ID: 3.18 × t 0.165 × 600 (1.25 in. × 0.065 in. × 19.7 ft)
Tube	Number of Tubes (ea) Dimension (cm)	4 OD: 0.952 × t 0.165 × 600 (0.375 in. × 0.065 in. × 19.7 ft)	4 OD: 0.952 × t 0.165 × 600 (0.375 in. × 0.065 in. × 19.7 ft)

the "reheat to cool" column represent extra heating requirements due to centrally cooling the supply air. The central cooling may occur when the economizer operates and does not necessarily translate to a chiller load.

The "system cool" column separates the cooling coil load into latent and sensible components. The column also presents the cooling accomplished by the economizer. This quantity is the outdoor airflow rate multiplied by the enthalpy difference between the outdoor air and return air when the economizer is operating. Its large column segment shows the significant contributions to cooling a properly working economizer can have.

Some important observations about system performance can be made from Figure 1. The annual fan energy use of the VAV system is about 40% of the CAV system. The fan savings determined by the simulation is consistent with measured values reported for VAV retrofits of CAV systems (Jagemar 1994). Reheating cool air makes up most of the system load on the boiler for the CAV system. The "reheat to heat" system load is much greater than the heat load due to thermal mixing. As expected, the "reheat to cool" energy is much reduced in the VAV systems. The significantly higher CAV system loads show the disadvantage of system designs based on noncoincident loads and constant airflow rate. The VAV system can respond more dynamically to loads.

The CAV to VAV retrofit not only reduces fan energy consumption but also significantly reduces cooling and heating energy use. This results from the interdependence of system cooling loads and heating loads on each other and on airflow rate. Additionally, the VAV retrofit substantially reduces system and plant equipment size requirements. For the location analyzed, the peak reheat load for the VAV system is about 75% of the CAV system load. The peak cooling coil load for the VAV system is about 65% of the CAV system load.

Improving System Design Using the Second Law

The low ratio of energy produced (building load) to energy consumed (plant energy) for heating in Figure 1 demands attention. While the VAV design is an improvement over the CAV, the first law efficiency for providing space conditioning to the building is still low. Insights for improving system performance through design and operational changes can be gained by considering the second law. Second law guidance aids in the detection and avoidance of unnecessary depletion of useful work in a process. Second law guidelines that are particularly relevant to HVAC distribution systems include (Sama 1995) the following:

1. Minimize the mixing of streams with different temperatures and pressures.
2. Do not discard heat at high temperatures to the ambient or to cooling water.
3. Do not heat refrigerated streams with hot streams.
4. Heat (or refrigeration) is more valuable the further the temperature is from ambient.
5. The larger the mass flow, the larger the opportunity to save (or waste) exergy.

Most of these considerations are common sense. Yet, in the design and operation of the CAV and VAV reheat systems, they are not adhered to. While there are many criteria other than thermodynamic performance for developing an acceptable design, any opportunities for reducing the depletion of useful work should be recognized when making design decisions.

The improvement of VAV performance to CAV can be explained by second law considerations. Airflow rates are lower for the VAV system, which reduces other second law errors including reheating cool air, discarding warm return air, and mixing streams at different temperatures. In addition, fan

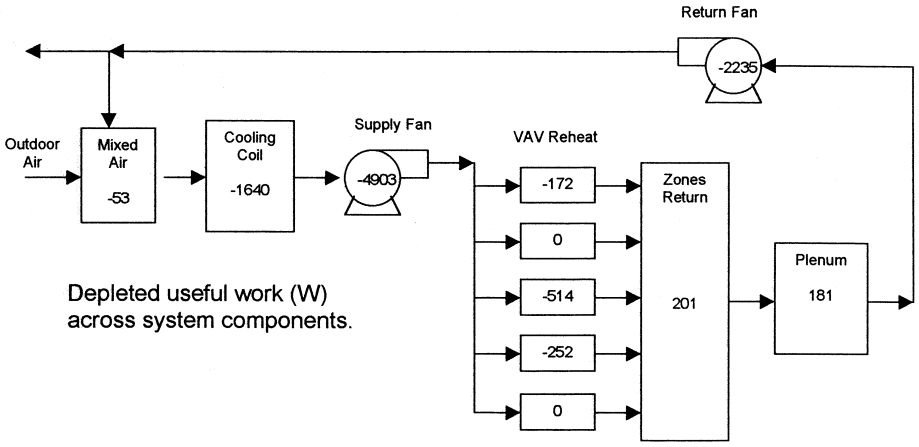

Notes:
-Steady state operation on 4/5 at 8 AM; ambient temperature of 16.6 °C (61.9 °F)
-Values for Zones Return and Plenum is exergy increase of air stream from internal gains

Figure 2 *Useful work depleted by VAV system during one hour.*

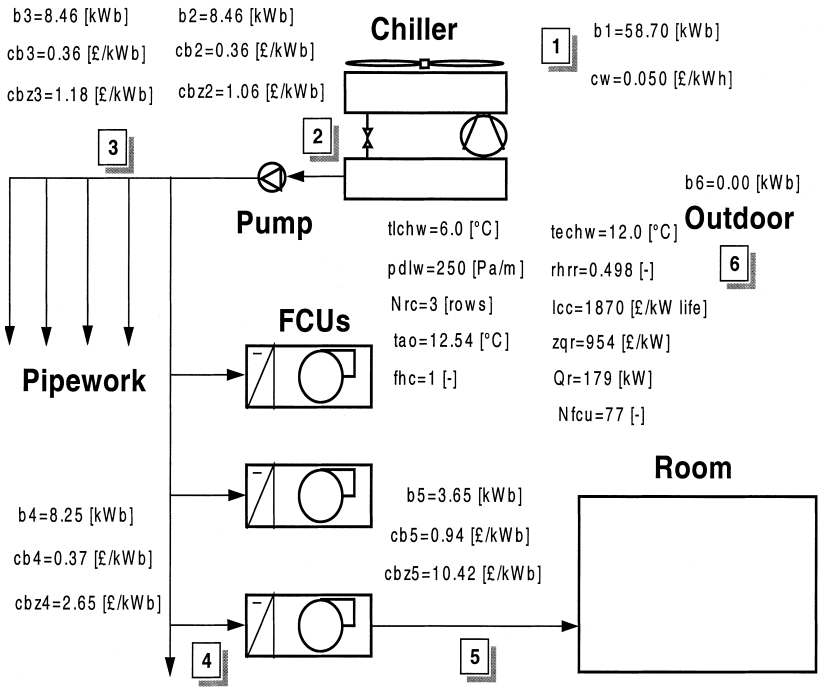

Figure 1 *Diagram of base design.*

room sensible heat ratio of 0.95, an economic life-cycle of 15 years, and an annual interest rate of 7.5%. It is recognized that wet coils have shorter lives than dry coils.

- Excluded from the analysis are the costs for cleaning coils in terms of whether they are dry or wet and the number of rows, filter replacements, and maintaining integrity of pipework insulation and vapor barriers.

Figure 1 indicates the specific exergy cost throughout the process from the chiller plant to the final product of building cooling, of the base system optimized as described previously. Two figures are given for each stage, whereby the cost flows are numbered 1 to 6, the c^{bz} figures that indicate the cost, taking into account the exergy and plant costs, whereas the c^{b} figures indicate these costs in terms of the exergy costs alone. The term *z* refers to capital costs, *w* to electric power and plant denominations. *Zqr* indicates the specific capital costs associated with the overall cooling system, and it is variable. Please refer to the nomenclature section, including subscripts and superscripts.

The analysis tool used was to determine the exergy costs, and exergy and capital costs and their relative cost increase, between the exergy flow (indicated in Figure 1) into and out of each plant, as indicated separately in Table 1. A careful analysis of these costs (last two columns in Table 1) indicates that the cost of chilled water has the highest increase, with respect to its incoming value, between cost flows 1 and 2. The next highest ratio is for the fan coil units between flows 4 and 5. In order to improve the overall system efficiency, an appropriate assessment of real achievable economic and exergy factors must be considered.

TABLE 1
Base Design Exergy and Flow Costs

Cost Flow (Figure 1)	Exergy, kW (*b*)	Exergy Cost, £/kWh (c^{b})	Exergy and Capital Cost, £/kWh (c^{bz})
1	58.7	0.05	0.05
2	8.46	0.36	1.06
3	8.46	0.36	1.18
4	8.25	0.37	2.65
5	3.65	0.94	10.42
6	0	N/a	N/a

Note: £1 is approximately 1.6 $U.S.

Based on the increase of costs, the independent system variables were selected for minimization of life-cycle costs. However, in terms of quality for people, the most important variable is the air OFF coil temperature, which has the potential to cause cold drafts. Therefore, the life-cycle costs were individually optimized by minimizing the objective function for different values of air OFF coil temperatures. To optimize the fan coil system design, the independent design variables selected were the leaving chilled water temperature, chilled water temperature difference, pipework friction loss, room relative humidity, number of coil rows, and number of fan coil units

- The optimization of the chiller had been limited by parameters imposed by the manufacturer. The manufac-